Exp Astron (2015) 40:183–214
DOI 10.1007/s10686-014-9427-9

ORIGINAL ARTICLE

Performances of JEM–EUSO: energy and $X_{\max}$ reconstruction

The JEM-EUSO Collaboration

Received: 17 June 2014 / Accepted: 13 October 2014 / Published online: 1 July 2015

Abstract The Extreme Universe Space Observatory (EUSO) on–board the Japanese Experimental Module (JEM) of the International Space Station aims at the detection of ultra high energy cosmic rays from space. The mission consists of a UV telescope which will detect the fluorescence light emitted by cosmic ray showers in the atmosphere. The mission, currently developed by a large international collaboration, is designed to be launched within this decade. In this article, we present the reconstruction of the energy of the observed events and we also address the $X_{\max}$ reconstruction. After discussing the algorithms developed for the energy and $X_{\max}$ reconstruction, we present several estimates of the energy resolution, as a function of the incident angle, and energy of the event. Similarly, estimates of the $X_{\max}$ resolution for various conditions are presented.

The full author list and affiliations are given at the end of the paper.

F. Fenu (✉)
Kepler Center for Astro– and Particle Physics (IAAT), Sand 1, 72076 Tübingen, Germany
e-mail: francesco.fenu@gmail.com

F. Fenu
Computational Astrophysics Laboratory, RIKEN (ASI), 2–1 Hirosawa, Wako, Japan

F. Fenu
Università degli Studi di Torino, Via Pietro Giuria 1, 10126 Torino, Italy

F. Fenu
Space and Astroparticle Group (SPAS), Universidad de Alcala, Alcala de Henares, Spain

A. Santangelo
Kepler Center for Astro– and Particle Physics (IAAT), Sand 1, 72076 Tübingen, Germany

D. Naumov
Joint Institute for Nuclear Research, Joliot Curie 6, Dubna, Moscow region, Russia

Keywords JEM–EUSO · Energy reconstruction · $X_{\max}$ reconstruction

1 Introduction

The Extreme Universe Space Observatory (EUSO) on–board the Japanese Experimental Module (JEM) of the International Space Station aims at the detection of ultra high energy cosmic particles from space [1]. JEM–EUSO is expected to observe ultra high energy (UHE) cosmic rays above and around the GZK threshold ($E \geq 4 \cdot 10^{19}$ eV), sensibly increasing the exposure with respect to the current generation of ground–based observatories. The expected exposure, virtually unattainable from ground, will most likely open a new observational window on the universe, given the high magnetic rigidity in such an energy range, and will unveil the sources of UHE cosmic rays and the mechanisms of their production. JEM–EUSO is also being designed to explore the neutrino and photon flux at UHE and, therefore, the discrimination capability of the mission for these particles, with respect to charged UHECRs, is critical. Details on the expected science of JEM–EUSO can be found in [2–5]. As stated in such publications the main objective of the JEM–EUSO mission consists in the study of the anisotropy of the extreme energy sky and in the identification of ultra high energy cosmic ray sources. Also the study of the trans–GZK region of the spectrum must be considered as a priority. The requirements to achieve such results are listed in [5] and include a ±30 % in energy resolution above $8 \cdot 10^{19}$ eV. JEM–EUSO has also several exploratory objectives like the separation of photons and neutrinos from hadrons. As stated in the above mentioned studies a resolution in $X_{\max}$ of ± 120 g/cm^2 at 10^{20} eV and 60 deg zenith angle is considered satisfactory for this purpose. On the other hand, the determination of the mass of the hadron primaries is not one of the JEM–EUSO objectives. Nevertheless, this remains a very appealing target for JEM–EUSO since it gives the chance to better constrain the production and propagation models. Efforts are therefore going on in the JEM–EUSO collaboration to explore also this aspect.

JEM–EUSO consists of a UV telescope sensitive in the 300–400 nm band, which records the fluorescence tracks generated by cosmic rays propagating in the atmosphere with a time resolution of 2.5 microseconds. The detector consists of an array of ~ 5000 Multi Anode Photomultipliers (PMT) organized in 137 PhotoDetector Modules (PDM). Each PMT is then subdivided in 64 pixels of 3×3 mm size, covering a field of view on ground of roughly 500×500 m. The detector therefore consists of more than $3 \cdot 10^5$ pixels, which cover a field of view of 500 km diameter. The structure of the focal surface can be seen in Fig. 1.

The instrument will observe the Earth's atmosphere at night from a height of about 400 km, with a field of view of about 60 degrees. The observed geometrical area will be of $\sim 1.4 \cdot 10^5$ km^2 and the surveyed atmospheric mass will amount to about $\sim 1.5 \cdot 10^{12}$ tons of air. The instrument payload is completed by an atmospheric monitoring system, which monitors the cloud coverage and cloud top height of the observed atmospheric scene, as well as, the optical depth of the atmosphere in the region of triggered events. For details of the instrument, we refer the reader to [6–8].

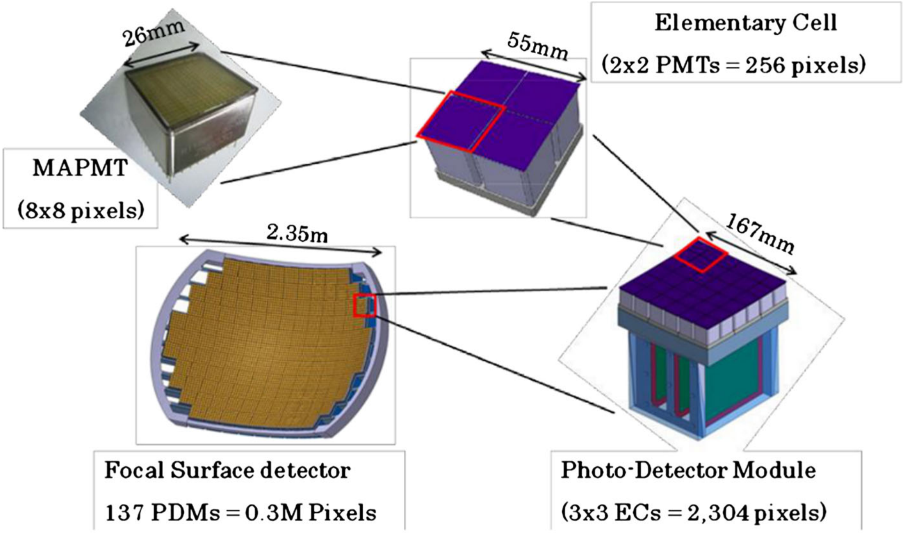

Fig. 1 The JEM–EUSO focal surface structure. From “Report on the phase A study 2010” of the JEM–EUSO collaboration [9]

For each observed event, the arrival time, arrival direction, energy, and $X_{\max}$ must be reconstructed to recover the full observational information.

In this paper, we present the algorithms developed to reconstruct the energy and $X_{\max}$ parameters for events observed by JEM–EUSO. These studies are key to understand the spectrum and nature of primary particles. The energy resolution also impacts a proper interpretation of the arrival directions map. After a detailed description of the algorithms, we present some preliminary estimates. Such results are only intended as a proof of the established reconstruction chain and are somehow conservative. Since we are continuing with the optimization of the algorithms and with the assessment of the systematics, better values for the JEM–EUSO energy and $X_{\max}$ resolution will be obtained in the future.

The Euso Simulation and Analysis Framework (ESAF) [10] is the simulation software developed in the framework of the ESA–EUSO mission. This software was developed as the mission simulation software to take care of the simulation of all the relevant processes from the shower simulation until the event reconstruction. The ESAF software has been readapted for the new JEM–EUSO instrument and has been used in the present study.

2 Energy and $X_{\max}$ reconstruction

The *PmtToShowerReco* is the energy and $X_{\max}$ reconstruction procedure developed to reconstruct events observed by JEM–EUSO. The reconstruction is structured in several subsequent steps, each of which performing a sub–task. The procedure is used for a first estimate of the shower parameters, like energy and $X_{\max}$. The method, already described in [11], has been significantly improved and, therefore, a detailed description of the algorithms has been done. A schematic view of this algorithm is given in Fig. 2.

The signal track selection The *PmtToShowerReco* receives the information in input on the timing and position for all the counts detected on the focal surface. For the analysis we only consider triggered events since this is the condition for data to be sent to ground. More details on the trigger logic can be found in [12]. The PDMs associated with a trigger (and neighboring PDMs) will therefore be sent to ground. In Fig. 3, an example of simulated data received from the instrument can be seen, including both signal and background. This is representing a shower event of $3 \cdot 10^{20}$ eV and 50 degrees zenith angle. At regular intervals, the shower spot crosses the PMTs gaps perpendicularly and, therefore, a decrease in the detected intensity has to be expected. In Fig. 4, the counts detected over the entire shower development time ($\sim$ 50 GTUs) are integrated. Here we only see the counts that originated from the shower unlike in Fig. 3. The signal (Fig. 4) cannot be separated from background since the JEM–EUSO instrument cannot determine whether a photon is originated from a shower or from airglow. Nevertheless, a clear concentration of signal is visible already on the raw data of Fig. 3.

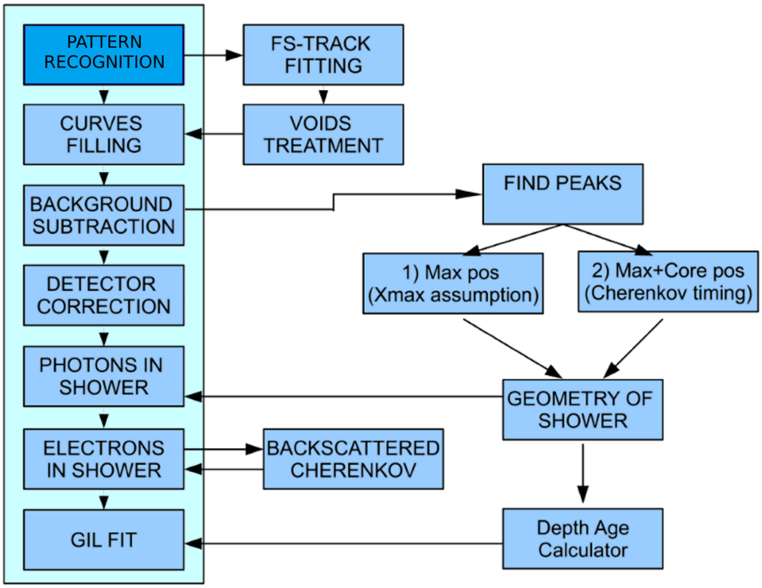

Fig. 2 A simplified view of the *PmtToShowerReco* reconstruction is given here. The input information is represented by the *blue box marker* with the title *PatternRecognition*. Here information, like the amount of counts for each time and position, is given. Following the *vertical path underlined in cyan*, the counts curve is transformed according to a series of correction factors which are applied in each step. Complementary operations are executed on the *right side* of the diagram

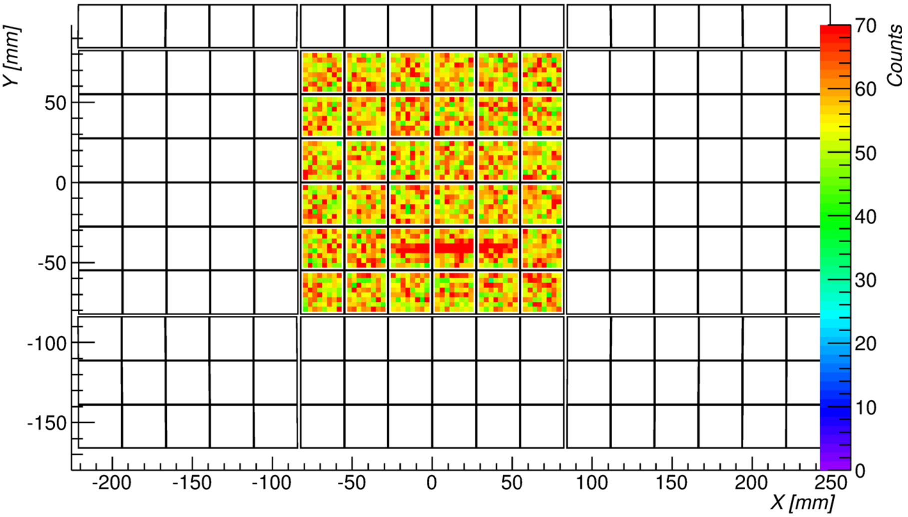

Fig. 3 The data received from the instrument. As can be seen here, background and signal photons cannot be distinguished. The *color scale* represents the integrated number of counts

In fact, the shower signal can be imagined as a spot moving on the focal surface with a speed equal to the projection of the shower speed. In Fig. 5, the temporal evolution of the track can be observed. The shower signal has been represented in colors depending on the photons arrival time. Five temporal windows, each of 10 GTUs (25 μs), have been identified. This particular shower is, therefore, clearly evolving to the right of the image for a time duration of roughly 50 GTUs.

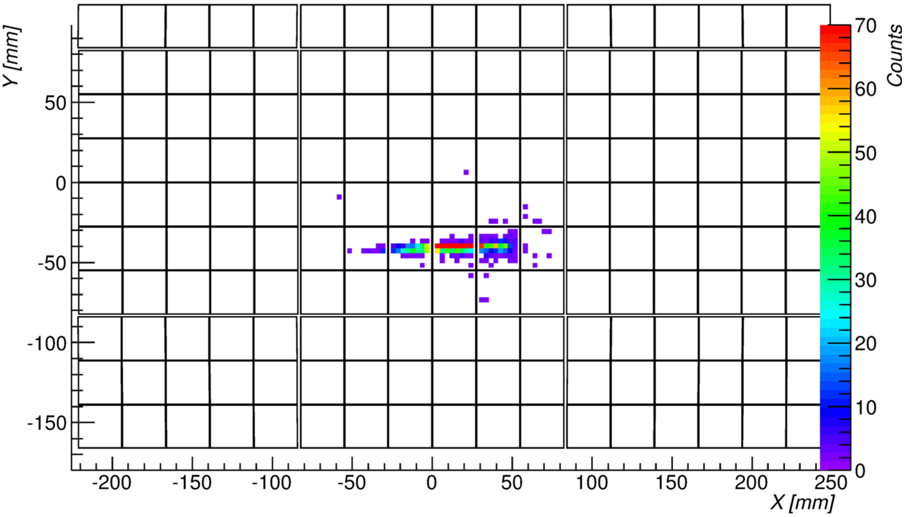

Fig. 4 The simulated track is shown here. We only see the counts originated by the *shower*. The *color scale* represents the integrated number of counts

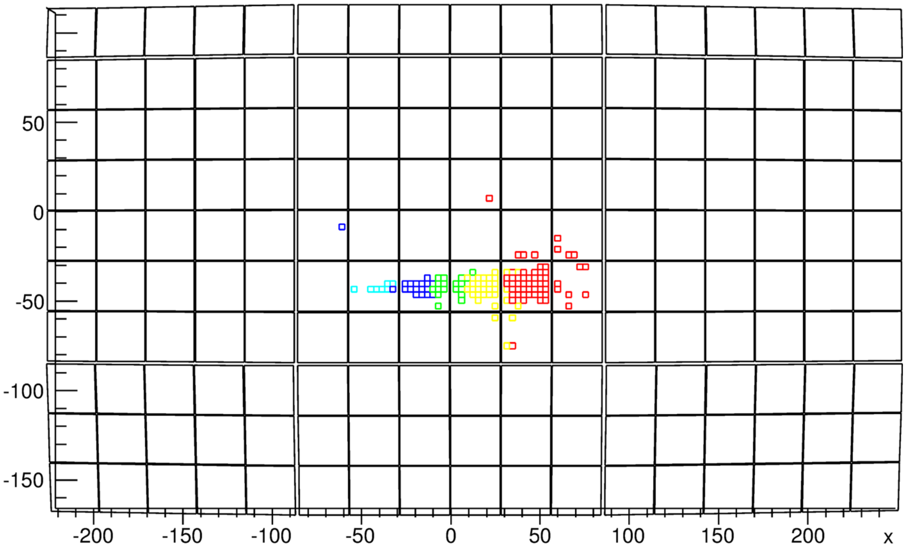

Fig. 5 The evolution in time of the shower simulated track. The *color scale* represents 5 different time windows in which simulated photons reach the detector

The first task of the reconstruction must be the identification of the pixels and GTUs with signal. Several algorithms have been developed for this purpose. In this work, two have been used, namely the *LTTPatternRecognition* and the *PWISE* algorithms [11, 13]. A detailed discussion of the two algorithms is out of the scope of this publication but both of them are looking for signal excesses concentrated in space and moving in a coherent way. As can be seen in Figs. 6 and 7, both such selections follow the real track shown in Fig. 4. On the basis of what was identified by the pattern recognition for each GTU, we calculate the center of mass of the spot. All the pixels whose center falls within a 3.5 mm radius are chosen for the construction of the signal curve. This choice has been made in order to select an area that is on average equal to the collection area of the *OpticsResponse* (See paragraph *The detector correction* for more explanations).

The signal curve reconstruction The first step of the *PmtToShowerReco* consists of the reconstruction of the so–called curve of counts, in other terms, the number of counts per GTU detected by the instrument. The information of the reconstructed track (based on Figs. 6 or 7) is read out and the timing for all the counts in the selected data is used to obtain the signal intensity as function of time.

In parallel, we calculate the average position for each time frame in order to assess possible signal losses due to focal surface voids. In fact, when the spot approaches the gaps between PMTs a part of it will fall onto a non sensible area of the detector. A decrease of the signal intensity then must be expected. Such loss will cause systematics in the energy reconstruction. Two possibilities are open for removing this problem. When the signal for a particular time frame is close to focal surface gaps, it must be either removed or corrected. In the present study, all the points falling within

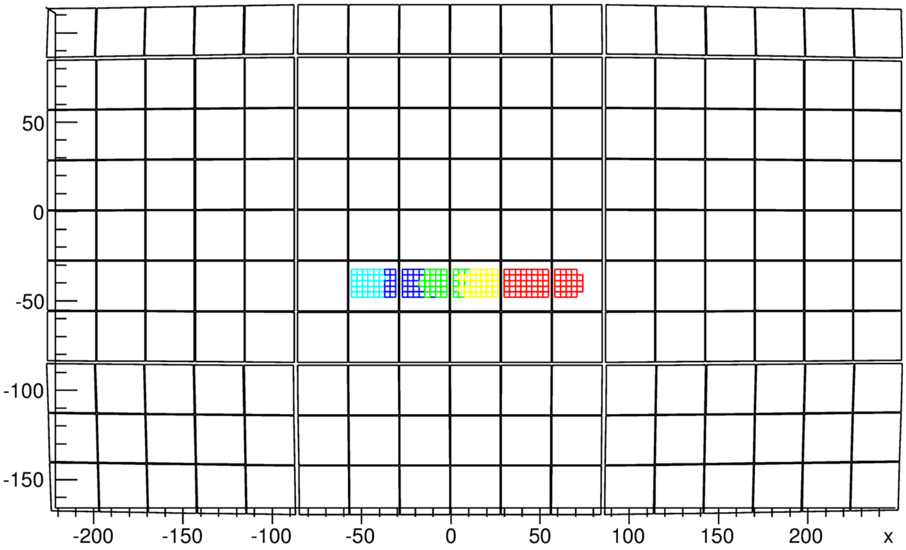

Fig. 6 The signal selection according to the *LTTPatternRecognition* algorithm. In *color scale*, 5 time windows each of 10 GTUs can be seen

3 mm from the gaps are removed since no sufficiently detailed spot parameterization has yet been developed. Such a radius is chosen, taking into account the projection of the shower lateral distribution, so that it will include most of the JEM–EUSO signal.

An essential step of the reconstruction chain is the correction of the background. Depending on the selected area, in fact, the background component must be subtracted from the signal intensity curve. In fact, the identification of the pixel–GTU with signal does not mean the identification of pure signal. Such pixel GTUs will still be contaminated by a certain amount of photons from airglow background. The knowledge of such a contamination can be achieved very easily by long time measurements of the diffuse Earth emission. The knowledge of the average background therefore allows the correction of a certain amount of counts each GTU. A constant background amount is subtracted for each selected pixel–GTU.

The counts curve is therefore built, according to the previously described selection, and the background is subtracted. An example of such a curve for the analyzed event can be seen in Fig. 8. In this figure, the reconstructed curve (points with error bars) is superposed with the simulated curve (continuous curve). As can be seen, the two curves are in good agreement except for the regions where gaps are present (gray areas).

The peak identification The identification of the maximum and Cherenkov peak of the reconstructed light curve is also critical. The search for these features is not trivial.

Depending on the zenith angle and on the nature of the diffusing surface,[1] the Cherenkov reflected component can be rather spread, implying a reduction

---

[1] The Cherenkov reflection will be modelled as a Lambertian reflector with an albedo of 5 %.

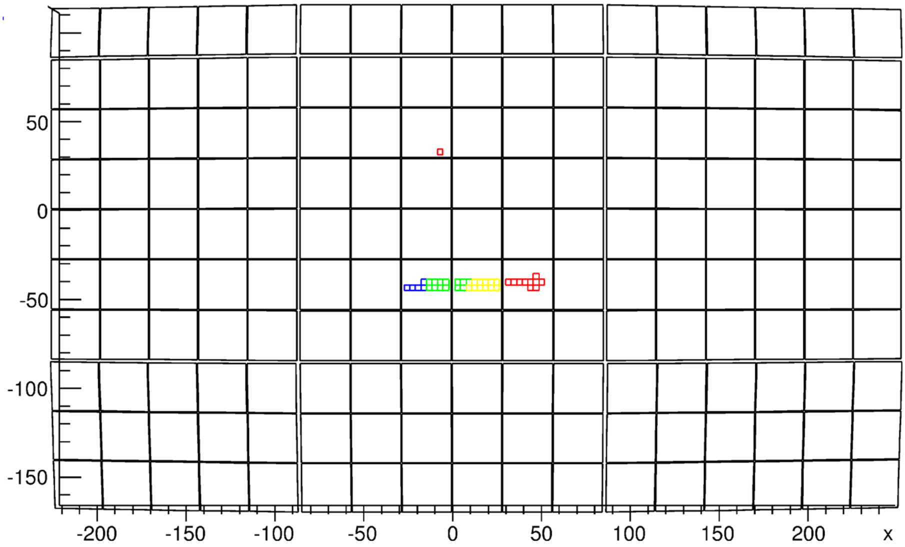

Fig. 7 The signal selection according to the *PWISE* algorithm. In *color scale*, 5 time windows each of 10 GTUs can be seen

of the signal to noise ratio. For these reasons, the recognition of a physically reasonable peak is not trivial, and not always possible, and requires a dedicated analysis. The algorithm takes into account the most common cases and tries to

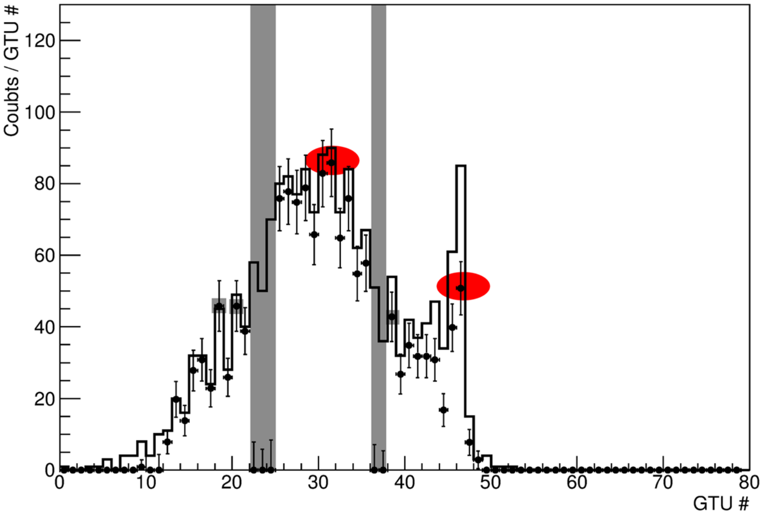

Fig. 8 The simulated (*line*) and reconstructed (*points*) detector counts curve. *Highlighted with squares*, are the bins recognized as peaks by the procedure. *Highlighted with ellipses*, are the peaks identified as Cherenkov and maximum. Two gaps can be observed as *shaded areas*. The current configuration sets the signal in the vicinity of a gap to zero. The simulated event has an energy of $3 \cdot 10^{20}$ eV and a zenith angle of 50 degrees

cope with them in order to recognize the highest fraction of events showing the Cherenkov mark.

A cleaning of the signal is necessary to avoid the detection of fake peaks, in particular, toward the later stages of the event, where the signal is low. In fact, especially for high zenith angles, events can be characterized by long tails due to the backscattering of the photons in atmosphere. For this purpose, a search in a ±2 window around each bin is done. If the bin is isolated, namely if more than 3 bins out of 5 are equal to zero, it will not be considered for the peak search. The isolated bin will still be considered if its intensity is over a certain threshold (10 counts), since it is unlikely that backscattering can generate such a strong, timely constrained bin.

As a next step, all peaks in the counts curve are identified. The peak is defined assuming that a bin is the maximum between the ±2 adjacent bins. In other words, if the bin is larger than (or equal to) the ±2 bins around it, it will be considered as a peak. Another requirement for a bin to be accepted as a peak is its amplitude. If the peak is at least of amplitude 10 counts, it will be accepted otherwise, it will be rejected. This is done in order to reduce fake peaks due to background fluctuations. We then analyze the detected peaks to find the temporal position of the Cherenkov mark and the maximum. After the cleaning described above, the last peak can usually be identified as a preliminary Cherenkov peak. However, cuts must be applied on the peak to reduce the probability of fake Cherenkov identification. For example, the duration of the shower after the preliminary Cherenkov is a valid selection parameter. In fact, the Cherenkov reflection peak should, in most cases, represent the end of the shower. The presence of significant amounts of light after the peak is most likely an indication of a fake Cherenkov reconstruction. This is happening in most of the showers with a zenith angle above 60 degrees. In such cases, any peak after the maximum could, in fact, be identified as preliminary Cherenkov.

A further selection criterion can be applied on the time separation between the Cherenkov and maximum. The knowledge of the reconstructed shower zenith angle [14] and the assumption of a shower parameterization will set constraints on the minimum time separation between maximum and Cherenkov. In fact, direction and a shower parameterization will turn into an estimate of the maximum altitude. Such an altitude will, therefore, translate into a minimum time separation between maximum and the impact on ground. Further criteria on the peak intensity can be chosen in order to minimize the risk of fake detection.

The maximum will be usually identified as the peak with the maximum intensity, excluding the preliminary Cherenkov. In the case that more maxima have the same amplitude, the average between the peaks GTU number is considered. Moreover, maxima near gaps are considered in a devoted way. In fact, if the most intense peak is in the vicinity of a gap it will most likely be affected by systematics. If strong secondary peaks are present (with at least 90 % the intensity of the maximum), the weighted average between their timing and the maximum will be calculated. This will be considered to be the best estimation of the maximum.

An example of peak search is given in Fig. 8 where the peaks are analyzed. As can be seen, the Cherenkov and maximum peaks have been correctly identified and

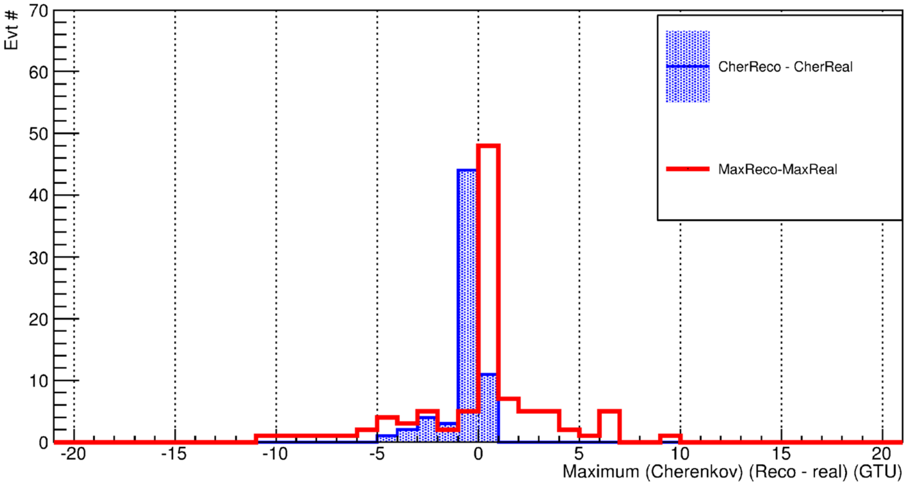

Fig. 9 The quality of the maximum and Cherenkov peaks reconstruction. Plotted here is the difference between reconstructed and simulated maxima and Cherenkov for 100 events

highlighted with red ellipses. Minor peaks have also been found and underlined with gray squares.[2] As can be seen, their vicinity to gaps makes it clear that peaks are more likely to occur in this situation. This, however, does not hamper the search for the maximum or for the Cherenkov peak. A preselection, excluding peaks near gaps, has not been performed to avoid loss of maxima or Cherenkov falling near the PMT boundary. Optimization work can be still done to reduce the number of gap–related peaks.

In Fig. 9, the evaluation of the quality of the peak search is given for 100 events of 10^{20} eV, 50 degrees. Here, we plot the reconstruction quality of the maximum and Cherenkov according to (1) and (2)

$$\Delta_{cher} = GTU^{reco}_{cher} - GTU^{simu}_{cher} \tag{1}$$

$$\Delta_{max} = GTU^{reco}_{max} - GTU^{simu}_{max} \tag{2}$$

The maximum distribution is centered on 0.2 and has an RMS of 3 GTUs. The Cherenkov peak is centered on -0.65 and has an RMS of 1 GTU. This shows how the maximum is more sensible on fluctuation and on the presence of gaps than the Cherenkov. Moreover, 65 events out of 100 have been recognized with Cherenkov while the maximum has been recognized in all 100 events.

The detector correction The photons curve on the focal surface is then reconstructed. To reach this step, we use a parameterization of the photo–detector, which includes the efficiency of the PMTs, the loss of the front end and the transmittance of the optical filter.

---

[2] A small note should be given on the peaks on GTUs 18 and 20. These peaks are identified given the very unlikely case of peaks of exactly the same amplitude within ± 2 GTUs. The condition chosen for a bin to be accepted as peak is $\geq$.

Following that, we correct the effects of the optics, taking into account the optics efficiency, using the *OpticsResponse* of ESAF. This map is produced with aid of a script run outside of the main reconstruction frame. In order to calculate the *OpticsResponse* map, several point sources are simulated following a set of predefined incident angles and wavelengths. The optics efficiency factor is calculated for each direction as in (3).

$$\varepsilon_{\rm opt} = \frac{\gamma_{\rm encirc}}{\gamma_{\rm opt}} \tag{3}$$

The so–called trigger throughput $\varepsilon_{\rm opt}$ is affected both by the performances of the optics and by the physical width of the shower [15], and is the ratio of the photons reaching the focal surface within a predefined collection area $\gamma_{\rm encirc}$, with respect to the photons incident on the pupil $\gamma_{\rm opt}$. The photons landing outside of the collection area have been considered not detectable since they are indistinguishable from the background. A collection area of 3 mm radius has been chosen in the present work. This choice is justified considering that most of the signal falls in a circular area of 3 mm radius. The center of this area is chosen as the point with the maximal photon density.

Other essential information is the mapping of the arrival directions as a function of the pixel identification number, namely the so–called *PixelAngleMap*. The *PixelAngleMap* allows the reconstruction of the arrival direction of the photons seen by any pixel. This map is also produced with the aid of a script run outside of the main reconstruction frame. The script produces a large amount of photons of various wavelengths diffusively shining on the pupil. The off–axis angle is chosen to vary continuously from 0 to well above the JEM–EUSO field of view (±45 degrees) to consider the effect of stray light. The wavelength is ranging from 250 to 500 nm. The distribution of arrival direction for all the photons landing on each pixel will be produced and its average will be saved in the *PixelAngleMap*.

The maps described above allow the calculation of an efficiency factor for each phase of the event development. This efficiency factor is needed to calculate the photon curve at the optics entrance. The final output of the chain is in fact an estimated *photon curve* at the entrance pupil. The simulated and the reconstructed photons curve on pupil can be seen in Fig. 10 for the same event shown above.

In Fig. 11 we can observe, as an example, the radial distance on the focal surface of the spot originated from a source in the field of view. More in detail we show here the dependence of the radial distance on the focal surface from the radial distance in the field of view. As can be seen, three series of data points are shown along the X, Y axis and along the diagonal. The detector shows a good axial symmetry at least if we exclude the side–cut section.

The shower's axis reconstruction At this stage, the luminosity of the shower must be calculated. For this purpose, we need to know the shower position as a function of time. This is necessary in order to estimate the distance of the shower from the detector and consequently, the total amount of photons produced. Given the total number of photons at the pupil and the $\frac{1}{d^2}$ flux decrease factor, it is possible to reconstruct the number of photons at the shower site. The knowledge of the shower position in

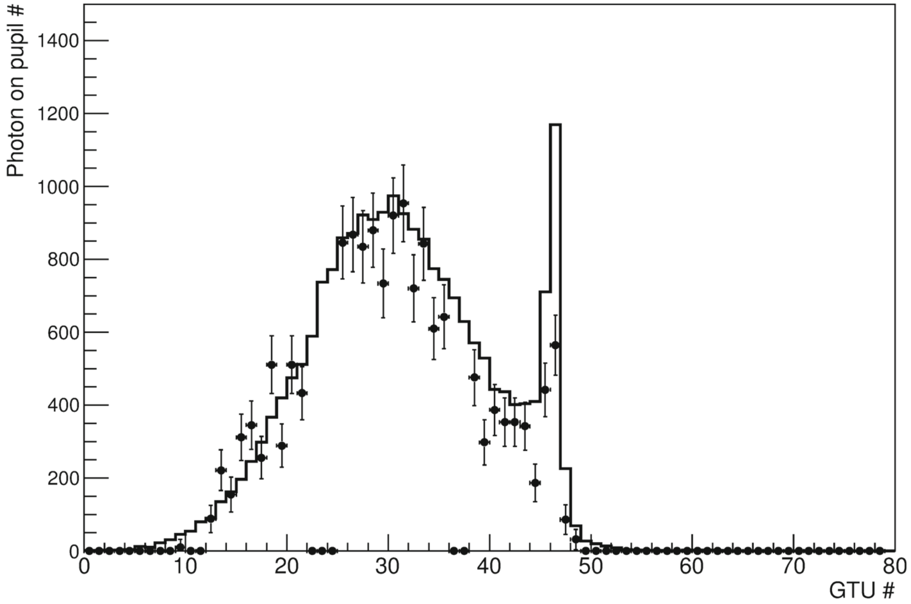

Fig. 10 The simulated (*line*) and reconstructed (*points*) pupil photon curve. The simulated event has an energy of $3 \cdot 10^{20}$ eV and a zenith angle of 50 degrees

the earth's atmosphere is also needed to properly apply all corrections relative to the atmospheric absorption and scattering.

To reconstruct the position of the shower in the atmosphere, we use two alternative procedures. The first makes use of the Cherenkov reflection mark, while the second assumes a parameterization for the depth of the maximum (X_{max}) and relies on the direction estimated with the angular reconstruction procedure [14].

The first method shown in Fig. 12 assumes the identification of a Cherenkov mark in the light curve. The time delay between the shower maximum and the Cherenkov mark allows the distance traveled by the shower to be calculated. This is easily understood from basic kinematics, considering that showers propagate at the speed of light. Knowing the projection of the maximum and of the Cherenkov mark, it is possible to infer the altitude of the maximum itself. In fact, the detection of the Cherenkov mark, in clear sky conditions, constrains the position of the shower at the ground level within a very narrow time window. In other terms, the timing and position of both peaks will efficiently constrain the zenith angle of the shower.

The second method (also called slant depth method) is schematically shown in Fig. 13 and relies on the prior reconstruction of the direction [14] and on the knowledge of the maximum projection onto the field of view. Given the dependence of the energy and X_{max} reconstruction from the angular resolution we report here for completeness a table taken from [14]. We see here the angular resolution for different zenith angles and energies on the whole field of view. In Fig. 13 of [14] the dependence of the angular reconstruction from the position in the field of view is reported (Table 1).

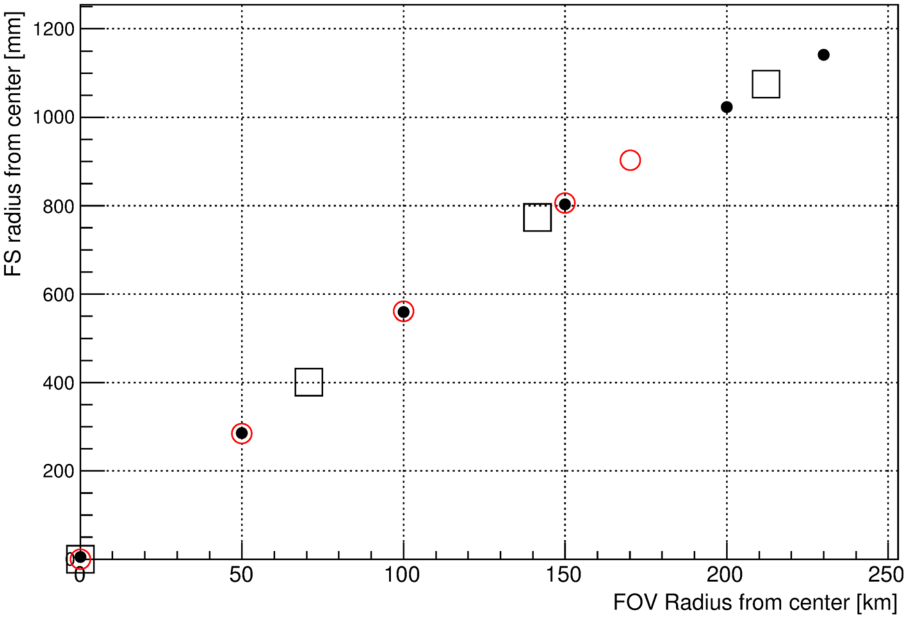

Fig. 11 The radial distance of a spot on the focal surface as function of the radial distance of a source in the field of view. Such distances are respectively measured in mm and km. As *black dots* we represent the radial distance along the axis $Y = 0$, as *red circles* $X = 0$ and as *black squares* $X = Y$. We represented the points (0,0) (50,0) (100,0) (150,0) (200,0) (230,0) (0,50) (0,100) (0,150) (0,170) (50,50) (100,100) (150,150) km

An $H_{\max}$ is determined according to the depth of the points in the projected maximum along the shower direction (see Fig. 13). Of course, $X_{\max}$ depends on the nature of the primary. Therefore, a distinction must be made between the assumed $X_{\max}^{\text{geo}}$ and the resulting $X_{\max}^{\text{fit}}$ obtained from the fit. We stress that the entire procedure must be iterated to obtain the best possible geometry reconstruction and get rid of the initial assumptions on $X_{\max}^{\text{geo}}$.[3] The results obtained through this method will be biased by the initial assumption on $X_{\max}^{\text{geo}}$. However, the energy sensibility to the bias is contained within 10 %, as long as, the altitude is reconstructed within 2 km accuracy. The $X_{\max}^{\text{fit}}$ must be treated more carefully, since a few hundred meters altitude bias can already result in a strong bias on the slant depth of the maximum.

The knowledge of the maximum position and shower direction allows the calculation of the shower position and slant depth for all times. The atmospheric profile (US Standard 1976 Atmosphere [16]) is used together with the reconstructed shower's

---

[3] A complete explanation on the iteration procedure is out of the scope of this publication. The iteration will be performed by variating the shower parameters obtained through the first reconstruction run. The reconstruction will be applied backward and the detector response obtained in this way will be compared with what originally detected by JEM–EUSO. The deviation of this test from the data will define a confidence interval in the parameter space and possibly deliver a better set of parameters than what was found in the first run.

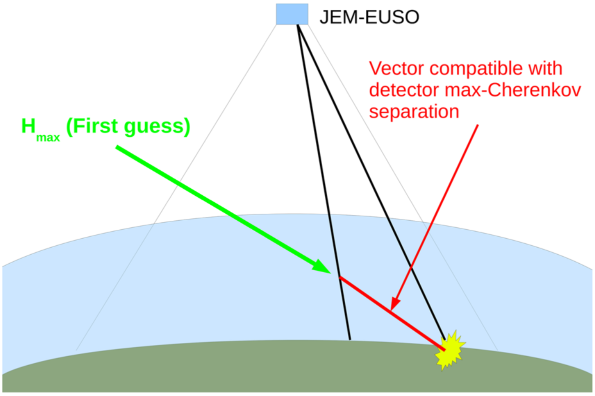

Fig. 12 The Cherenkov H_{max} reconstruction method. This algorithm requires the reconstruction of both maximum and Cherenkov peak. The separation time between the two events at the detector and the altitude of the ground gives information on the altitude of the maximum

direction and position to integrate the atmospheric density until the top of the atmosphere. We also estimate the shower age from the information on the position of the maximum.

The shower's luminosity reconstruction Knowing the position of the shower as function of time and the shower's age, we can estimate the energy distribution of the secondary electrons. We use, for this study, the parameterization from [17]. The knowledge of the produced photon energy spectrum is then used for the estimate of the scattering and absorption in atmosphere. At this stage, the shower luminosity estimation is concluded. In fact, by knowing the position of the shower inside the atmosphere and the produced spectrum, the modelization of the transmittance can be performed. For this purpose, the standard *lowtran* software has been chosen [18]. In

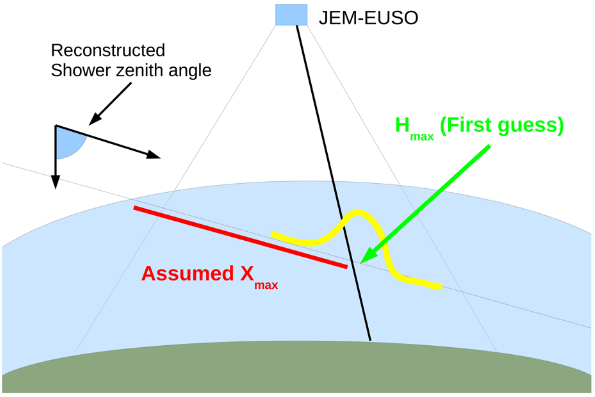

Fig. 13 The slant depth H_{max} reconstruction method. This algorithm requires the reconstruction of the shower direction and an assumption on the slant depth of the maximum. This set of parameters constrains the altitude of the maximum in atmosphere

Table 1 the angular resolution from [14] for different zenith angles and energies

Zenith angle (deg)	$5 \cdot 10^{19}$ eV	$7 \cdot 10^{19}$ eV	10^{20} eV	$3 \cdot 10^{20}$ eV
30	4.5	4.5	4.0	3.5
45	4.0	3.0	2.7	2.0
60	2.7	2.5	1.0	0.7
75	1.3	1.2	0.7	0.5

We show the separation angle in degrees between simulated and reconstructed direction. The values plotted here represent the angle in degrees which includes 68 % of the events

Fig. 14, the reconstructed and simulated shower luminosity can be seen for the usual $3 \cdot 10^{20}$ eV 50 degrees event.

The shower profile reconstruction and fit After calculating the luminosity as function of location and slant depth, the shower profile is reconstructed. The knowledge of the fluorescence [19] and Cherenkov[4] yield then allows the reconstruction of the electrons curve of the shower. Unfortunately, no distinction is possible on whether the reconstructed photons are originating from fluorescence or backscattered Cherenkov light (See Fig. 15 for an explanation of the signal composition). An iterative procedure is being developed in order to disentangle the two components . Another possibility is the one described in [20]. However, the present results are not including such corrections and the final result will be affected by an overestimation of the energy due to such contamination. The systematics brought by the missing correction of the Cherenkov contamination[5] have been assessed and will be corrected later.

The obtained electron curve is fitted to obtain the energy and $X_{\max}$ parameters. In the present study, we have chosen the GIL function [21–24] for the fit, but any other function can be applied. The GIL function is shown in (4) and (5). Here E represents the energy, $t = \frac{X}{37.5g/cm^2}$ and A is the particle mass. Such functions have been used since they depend just on two parameters, namely the energy and the particle mass. This removes shower's width fluctuations and makes the development of the algorithms easier. Efforts are ongoing to include more complex parameterizations.

$$N_e = \frac{E}{1.45 \cdot 10^9 eV} \cdot e^{t - t_{max} - 2 \cdot t \cdot ln \frac{2}{1 + \frac{t_{max}}{t}}} \tag{4}$$

$$t_{max} = 1.7 + 0.76 \cdot (ln \frac{E}{8.1 \cdot 10^7 eV} - lnA) \tag{5}$$

The guide event shown above is also represented in Fig. 16, where real and reconstructed profiles are plotted together with the fit on the reconstructed points.

---

[4] According to the standard theory the Cherenkov yield is equal to $C_{\mathrm{Y}}(E, h) = 2\pi\alpha \left(2\delta - \left(\frac{m_e c^2}{E}\right)^2\right) \left(\frac{1}{\lambda_{\min}} - \frac{1}{\lambda_{\max}}\right)$ where α is the fine structure constant, δ is n-1 (n is the refractive index), E the electron's energy, $\lambda_{\min}$ and $\lambda_{\max}$ are the integration extremes.

[5] The backscattered component is therefore not distinguishable from fluorescence and has to be corrected.

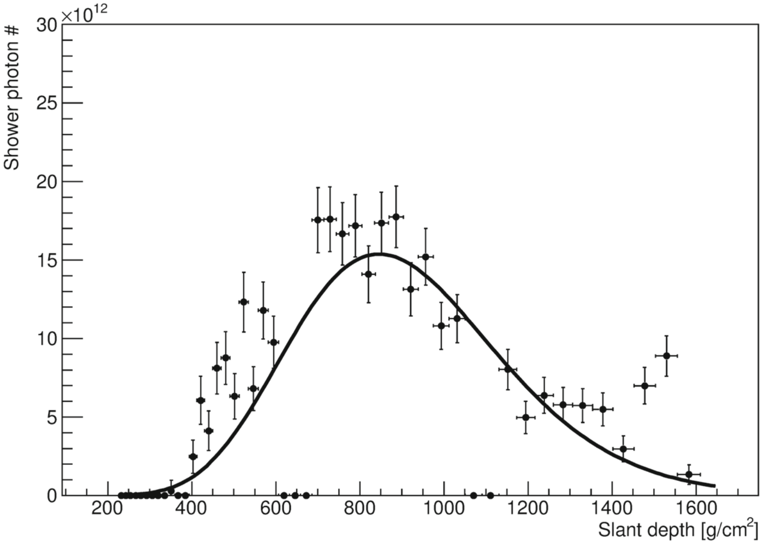

Fig. 14 The simulated (*line*) and reconstructed (*points*) shower photon curve (*shower luminosity*). The simulated event has an energy of $3 \cdot 10^{20}$ eV and a zenith angle of 50 degrees

We run the fit algorithm only on the points which are above a certain threshold in order to avoid the contamination of the result with the background dominated points. Furthermore, we select those points inside a window around maximum. This is done to exclude the Cherenkov peak.

The procedure described above and summarized in the diagram of Fig. 2 can be summarized with the following (6).

$$\begin{aligned}\frac{dN_{\mathrm{pe}}}{dL} = & \int_{\lambda_{\min}}^{\lambda_{\min}} \{N_{\mathrm{e}}(X(L), A, E)\epsilon_{\mathrm{FY}}^{\lambda}(H(L), s(L))\frac{1}{4\pi} \\ & + \Psi_{\mathrm{CH}}(\lambda, \overrightarrow{P}(L))\}\frac{A_{\mathrm{opt}}\cos\theta}{R^2}T_s(\lambda, \overrightarrow{P}(L), \overrightarrow{D}) \\ & \cdot T_{\mathrm{a}}(\lambda, \overrightarrow{P}(L), \overrightarrow{D})\epsilon_{\mathrm{opt}}(\lambda, \theta, \phi)T_{\mathrm{BG3}}(\lambda)\epsilon_{\mathrm{PMT}}(\lambda)\epsilon_{\mathrm{FE}}d\lambda \end{aligned} \tag{6}$$

The equation shows the amount of counts detected by JEM–EUSO for every element dL of the shower development. This number depends on the number of electrons in the shower $N_{\mathrm{e}}(X(L), A, E)$, parameterized as function of the energy E, on the atomic mass A and of the single step slant depth. $\epsilon_{\mathrm{FY}}^{\lambda}(H(L), s(L))$ is the fluorescence yield (in differential notation for each wavelength) which depends both on altitude and on the age of the shower. The dimension of the entrance pupil is expressed by the area A_{opt} which also includes a $\cos(\theta)$ factor to take into account the photons arrival direction. The efficiency of the detector is given by $\epsilon_{\mathrm{opt}}(\lambda, \theta, \phi)$, $\epsilon_{\mathrm{PMT}}(\lambda)$, ϵ_{FE} and $T_{\mathrm{BG3}}(\lambda)$ which respectively represent the throughput efficiency of the optics, the detector efficiency of the PMT, the losses of the front end electronics and the transmittance of the optical adaptor. Finally, the Rayleigh and ozone absorption are considered in $T_{\mathrm{s}}(\lambda, \overrightarrow{P}(L), \overrightarrow{D})$ and $T_{\mathrm{a}}(\lambda, \overrightarrow{P}(L), \overrightarrow{D})$, which depend

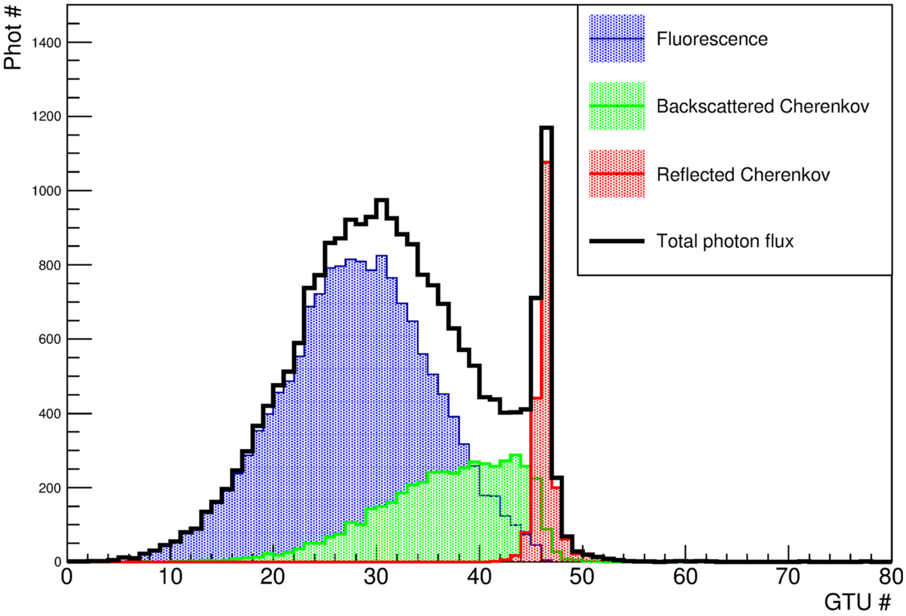

Fig. 15 The *curve* of photons at the pupil. In *different colors*, we show the different components of the *light curve*. In *blue*, we can see the direct fluorescence, *in green*, we can see the backscattered Cherenkov and, *in red*, we see the reflected Cherenkov. As *black line*, we see the total signal. The simulated event has an energy of $3 \cdot 10^{20}$ eV and a zenith angle of 50 degrees

on wavelength, shower and detector position. The function must be integrated from the minimum to the maximum wavelength and depends on the position which the shower occupies for each dL.

A specific treatment is needed to estimate the Cherenkov contamination $\Psi_{\text{CH}}(\lambda, \overrightarrow{P}(L))$. In (7), the additional component (in counts) due to Cherenkov and for each shower step is given:

$$\begin{aligned}\Psi_{\text{CH}}(\lambda, \overrightarrow{P}(L)) = &\int_0^L [N_e(X(l), A, E)\epsilon^{\lambda}_{\text{CH}}(H(l), s(l)) \\ &\cdot T_{\text{s}}(\lambda, \overrightarrow{P}(l), \overrightarrow{P}(L))T_{\text{a}}(\lambda, \overrightarrow{P}(l), \overrightarrow{P}(L))]dl \\ &\cdot(-\dot{T}_{\text{s}}(\lambda, \overrightarrow{P}(L))dl)\alpha_{anys} \qquad (7)\end{aligned}$$

What can be seen here is the integral from 0 to the actual shower longitudinal development of the whole propagating Cherenkov photon population. The number of electrons for each of the past steps of a shower $N_{\text{e}}(X(l), A, E)$ has to be considered together with the Cherenkov yield $\epsilon^{\lambda}_{\text{CH}}(H(l), s(l))$ integrated over the secondary energy spectrum. For each of the dl elements, the produced photons must be carried to the L point. The propagation is affected by losses $T_{\text{s}}(\lambda, \overrightarrow{P}(l), \overrightarrow{P}(L))$ $T_{\text{a}}(\lambda, \overrightarrow{P}(l), \overrightarrow{P}(L))$ respectively for scattering and ozone absorption. The derivative on dl of the scattered fraction $(-\dot{T}_{\text{s}}(\lambda, \overrightarrow{P}(L)))$ calculated at the L position multiplied by the differential dl describes how much of the transmitted light is scattered

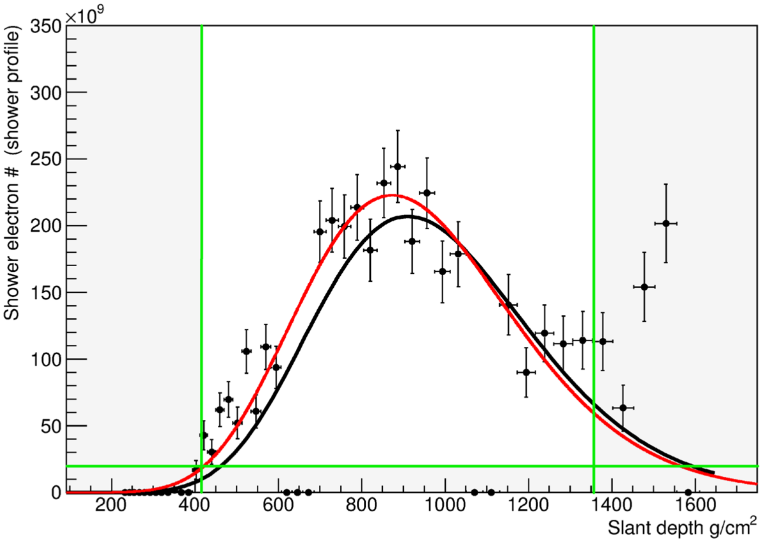

Fig. 16 The simulated (*black line*) and reconstructed (*points*) shower electron curve. As a *red line*, the GIL fit can be observed. The simulated event has an energy of $3 \cdot 10^{20}$ eV and a zenith angle of 50 degrees. The reconstructed parameters for this fit are $3.22 \cdot 10^{20}$ eV and 873 g/cm^2 (whereas the real $X_{\max}$ was 915 g/cm^2). The χ^2 per event is 0.905. The *shaded areas* show the points which are excluded from the fit

in the interval dl. It is well known that the Rayleigh scattering is not isotropic and, therefore, a component α_{anys} must account for the asymmetry of the scattered photons.

The systematics estimation The biases on the reconstructed parameters have also been analyzed in detail. Samples of events have been simulated in fixed conditions and reconstructed. Each of the previously described reconstruction steps has been therefore compared with the corresponding step in the simulation framework. In other terms, we perform a comparison between the model of the reconstruction and the Montecarlo. This is done to test the quality of the modeling with respect to the simulation.

We can, for example, take any of the Figs. 8, 10, 14 or 16 and calculate the correction factor applied in any of the reconstruction steps and compare it with the simulation. In the first case, for example, we would be calculating for each GTU the ratio between the reconstructed curves of Figs. 14 and 16 (the points) . Following that, we compare this ratio with the ratio between the continuous lines which represent the simulated curves. This expresses the deviation of a particular reconstruction step from the simulation. A schematic visualization of this process can be seen in Fig. 17.

Let us consider the simulation branch of Fig. 17. Being $N^{n}_{\mathrm{sim}}(t, \mathrm{evt})$ and $N^{n-1}_{\mathrm{sim}}(t, \mathrm{evt})$ the number of counts at the steps n and n - 1 for a time t and event evt, we define $\epsilon_{\mathrm{sim}}(t, \mathrm{evt})$ as the "efficiency" factor for an event evt, at the time t and

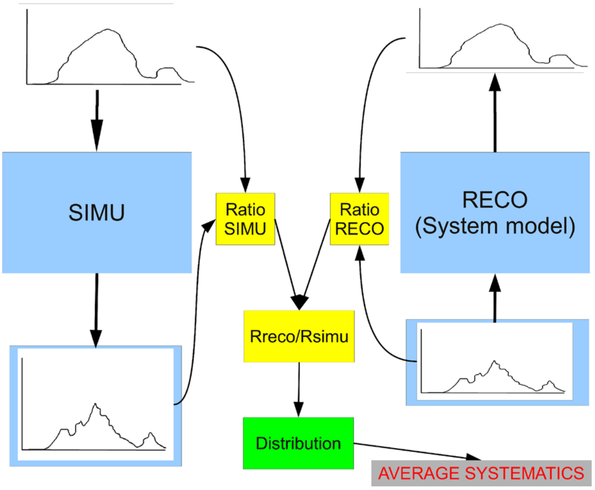

Fig. 17 The logic of the systematic estimation algorithm. A generic step is depicted. The ratio between input and output will be calculated for both reconstruction and simulation. The discrepancy of each reconstruction step from the simulated will be estimated for each event. The median on the distribution of the deviations will be defined as systematics (see *gray box*)

between the simulation steps n and n - 1.

$$\epsilon_{\text{sim}}(t, \text{evt}) = \frac{N^{n}_{\text{sim}}(t, \text{evt})}{N^{n-1}_{\text{sim}}(t, \text{evt})} \tag{8}$$

In the same way for the reconstruction branch, we define $N^{m}_{\text{reco}}(t, \text{evt})$ and $N^{m+1}_{\text{reco}}(t, \text{evt})$ which represent the number of counts at the steps m and m + 1, for event evt and time t. This brings us to the definition of the factor $\epsilon_{\text{reco}}(t, \text{evt})$ representing the correction factor applied between the mth and mth+1 reconstruction steps instead.

$$\epsilon_{\text{reco}}(t, \text{evt}) = \frac{N^{m}_{\text{reco}}(t, \text{evt})}{N^{m+1}_{\text{reco}}(t, \text{evt})} \tag{9}$$

Both n and m are indexes chosen to identify the simulation–reconstruction step and they are chosen from 0 to $\text{N}_{\text{max}} = \text{M}_{\text{max}}$. The index is defined in order to follow the “flux” of the operations. For this reason, n goes from shower to detector while m from detector to shower. Therefore, n must be defined to be equal to N_{max} - m (or M_{max} - m) in order to guarantee the correspondence between simulation and reconstruction steps. The ratio between the two factors is then mediated over all the event GTUs

$$\Delta^{k}(\text{evt}) = \frac{\sum_{t=0}^{t_{\max}} \frac{\epsilon_{\text{reco}}(t,\text{evt})}{\epsilon_{\text{sim}}(t,\text{evt})}}{t_{\max}} \tag{10}$$

giving the average bias of the single event for a specific condition k (for example angle, energy, primary type, position...). For a fixed condition k, a sample of events has been simulated and the $\Delta^{k}(\text{evt})$ factor calculated. The median of the distribution of the $\Delta^{k}(\text{evt})$ factor has been assumed to be the bias of the reconstruction on a particular step for a condition k. This estimation has been performed in different conditions and for all the correction steps applied in the reconstruction. This is the case for the focal surface (FocalSurf), optics (Opt), atmospheric transmission (Transmitt) and fluorescence yield (FluorYield) of Table 2. The factor (CTSsel), on the other hand, represents the collection inefficiency. This is simply calculated as the mediated ratio between reconstructed and simulated counts curve.

$$\Delta^{k}_{CTS}(\mathrm{evt}) = \sum_{t=0}^{t_{\max}} \frac{CTS_{\mathrm{reco}}(t, \mathrm{evt})}{CTS_{\mathrm{sim}}(t, \mathrm{evt})} \tag{11}$$

The factor $CTS_{\mathrm{reco}}(t, \mathrm{evt})$ represents the reconstructed counts curve while the $CTS_{\mathrm{sim}}(t, \mathrm{evt})$ represents the simulated. This ratio is then mediated over all the GTUs. The median over all the $\Delta^{k}_{CTS}(\mathrm{evt})$ will finally be put in Table 2 (under CTSsel) to represent how much of the simulated shower signal can be collected by the reconstruction algorithms in the condition k.

The contribution of the backscattered Cherenkov and the systematics of the geometrical uncertainties have been also estimated. In fact, in the standard configuration for the systematics study, the Cherenkov backscattering has been deactivated. In the same way, the reconstruction of the geometry is not considered and the reconstruction is performed with the simulated geometry. In this way, we try to disentangle different sources of systematics. We, therefore, simulate a sample of events in the same condition as in the standard case, but with the backscattered Cherenkov. The same is done for the geometrical reconstruction, where the sample is reconstructed using the reconstructed geometry. The ratio between the reconstructed energy obtained in standard condition and the new values are assumed to be the systematic brought by the non correction of the backscattered Cherenkov or by the geometry reconstruction. In (12), the reconstructed energy $E^{*}_{\mathrm{reco}}(evt)$ is obtained by using either the reconstructed geometry or by including the backscattered Cherenkov, while the $E^{**}_{\mathrm{reco}}(evt)$ is the standard case with no backscattered Cherenkov and reconstruction performed

Table 2 An example of the reconstruction bias is shown here

Zenith (deg)	CTSsel	FocalSurf	Opt	Transmitt	FluorYield	CherBack	GeoReco	Total
30	0.97	1.03	0.95	0.98	0.99	1.23	1.06	1.33
45	0.94	1.02	0.95	0.99	0.99	1.16	1.06	1.21
60	0.92	0.99	0.96	1	0.99	1.09	1.06	1.13
75	0.87	1	0.95	1.01	0.99	1.02	1.03	0.96

The chosen energy is 10^{20} eV, the events are impacting in the central part of the field of view (namely in the inner (±20, ±20) km) and the ϕ angle has been chosen from 0 to 360 degrees. The event zenith angle (θ), the bias on the signal selection (CTSsel), on the detector efficiency correction (FocalSurf), on the optics (Opt), on the transmittance (Transmitt), on the fluorescence yield (FluorYield), on the overestimation because of the backscattered Cherenkov (CherBack) and on the uncertainty because of the geometrical reconstruction (GeoReco) are represented in the columns. Total represents the product as shown in (13) with real geometry.

$$\Delta^{k}_{geo./backscatt.}(\text{evt}) = \frac{E^{*}_{\text{reco}}(evt)}{E^{**}_{\text{reco}}(evt)} \tag{12}$$

The median over the factors for all the events evt will be calculated and again reported in Table 2 (CherBack and GeoReco).

The Total factor is calculated as shown in (13) and represents the total systematic effects which have been identified.

$$\begin{aligned} Total &= CTSsel \times FocalSurf^{-1} \times Opt^{-1} \times Transmitt^{-1} \times FluorYield^{-1} \\ &\quad \times CherBack \times GeoReco \end{aligned} \tag{13}$$

This factor is the product of all the biases but has some of them in the denominator. This is due to the fact that such factors represent the deviation of the correction factor from the Montecarlo. The correction is always applied at the denominator and, therefore, an overestimation of the correction leads to an underestimation of the reconstructed energy.

More details can be found in [25] but one example is shown in Table 2 where several samples of 8000 events impacting near the center with different zenith angles and energy 10^{20} eV has been chosen. As can be seen, the algorithm we developed is affected by systematics which are generally within a 10 %. A notable exception is represented by the Cherenkov backscattered. Contamination can exceed the 20 %. This is expected since we are not performing any Cherenkov correction for the time being. In this way, the energy will be overestimated but the amount of additional light due to backscattering can be easily determined. The backscattered Cherenkov contamination is strongly influenced by the Rayleigh scattering anisotropy. In fact, being that the emission is stronger along the photon propagation axis, the contamination will be stronger for vertical events. Another evident pattern of Table 2, is the worsening collection capability of the algorithms at the highest zenith angles. This is due to the increasing lateral width of the shower at such angles. The spot will therefore be broader for horizontal showers. The fixed collection area we are assuming will lose efficiency when the spot increases in size. Efforts are going on to solve this discrepancy with a better spot parameterization.

Despite the detailed study on the systematics, we still have a residual of 4–8 % overestimation on all the inclinations. The final energy will be overestimated even after correcting the systematics of Table 2. The systematic study has been performed only in limited conditions. The corrections on all the samples of different energy, zenith angles and field of view positions are still underway and will require extrapolations to correct intermediate conditions as well. For this reason, we decided to represent the preliminary results as resolutions and to neglect (for the moment) the systematic shift for both the energy and the $X_{\max}$.

3 Energy resolution

Using the reconstruction procedure discussed in the previous Chapter, a study on the energy resolution of the JEM–EUSO mission has been performed for different zenith angles and different energies. The impact point is selected in the central part of the field of view (namely in the inner (±20, ±20) km). Showers are generated according to the GIL parameterization. We simulated 8000 events for each point and we applied quality cuts DOF> 4, χ^2/Ndf < 3 on all the conditions. In Figs. 18 and 19, we show the energy reconstruction performances for the slant depth and Cherenkov method, respectively. To estimate the quality of the reconstruction, we defined the parameter R for each event as in (14).

$$R = \frac{E_{reco} - E_{real}}{E_{real}} \tag{14}$$

The distribution of the R factor for all the events which survived the cuts has then been fitted with a Gaussian curve. The σ parameter has been reported here. As said before, we ignored the average of the distributions given the non completeness of the systematics study. An example of the R distribution arising from the condition 10^{20} eV, 45 degrees has been shown in Fig. 23. We also show here the Gaussian fit on this distribution.

As can be seen in Fig. 18, the energy resolution tends to improve toward the higher zenith angles. The resolution also tends to improve with the increasing energy due to the better quality of signal for the high energy events. Generally, the slant depth method will always have a resolution under 20 %. At the most extreme energies, the resolution reaches 10 % or even lower.

In Fig. 19, the energy resolution obtained with the Cherenkov method is shown. Again, the highest energies allow the best performances, while a clear improvement depending on the zenith angle cannot be seen anymore. This is due to the worsening

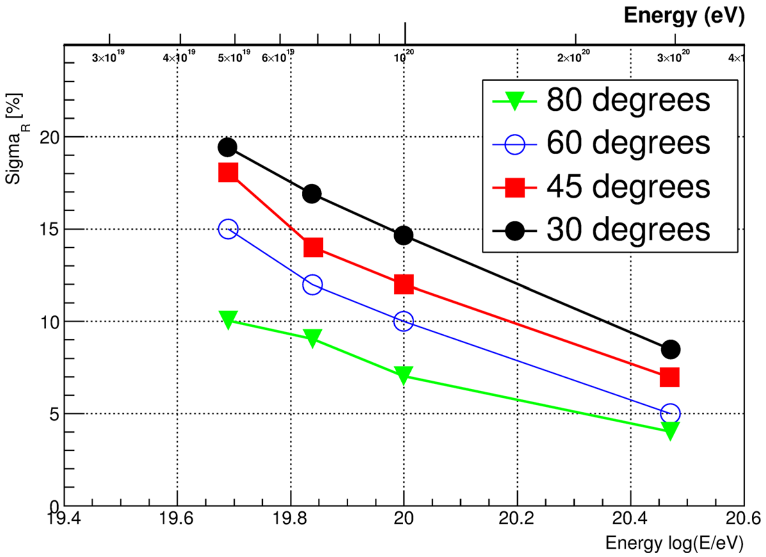

Fig. 18 The σ_R factor, namely the sigma on the distribution of all R (multiplied by 100), is shown here. Here, we plot the results for various zenith angles and energies. All the events are impacting in the central part of the field of view (namely in the inner (±20, ±20) km). The geometry has been reconstructed with the slant depth method

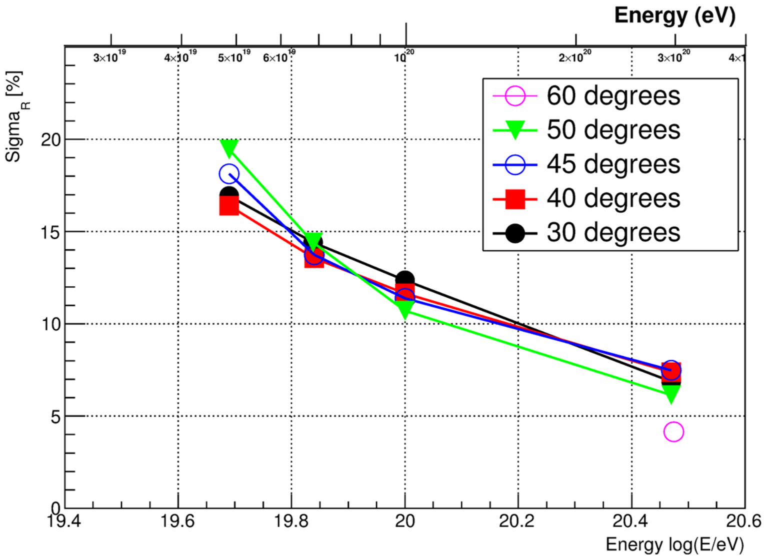

Fig. 19 The σ_R factor, namely the sigma on the distribution of all R (multiplied by 100), is shown here. Here we plot the results for various zenith angles and energies. All the events are impacting in the central part of the field of view (namely in the inner (±20, ±20) km). The geometry has been reconstructed with the Cherenkov method

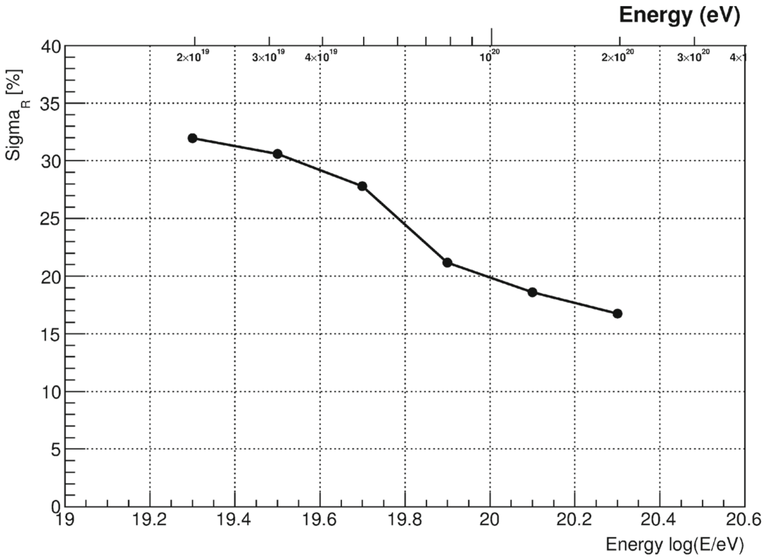

Fig. 20 The energy reconstruction performances are shown here for the all–event sample. The *points* represent the σ_R value (multiplied by 100). The sample with cuts DOF>4, $\chi^2/\mathrm{Ndf} < 3$ is shown here

quality of the Cherenkov peak at the highest zenith angles. In fact, the Cherenkov peak will be much more difficult to recognize at the large zenith angles due to the larger spread of this reflection spot. Moreover, because of this reason, the Cherenkov method cannot be extended above 50–60 degrees. The Cherenkov reconstruction can be extended at maximum at 60 degrees just for the highest energy events. In such cases, in fact, the strong Cherenkov signal will still allow the discrimination from background despite the high zenith angle. The lowest energies already show a loss of quality at smaller zenith angles.

Notably, both slant depth and Cherenkov method give comparable performances under all the conditions. Such methods can be also used as a valid cross check since they are totally independent from each other.

In Fig. 20, the energy resolution, estimated using the slant depth method, is shown for events distributed on the whole field of view namely in the range (±270, ± 200) km and for energies in the range $2 \cdot 10^{19}$–$2 \cdot 10^{20}$ eV. The events have zenith angles between 0 and 90 degrees distributed as $\sin(2\theta)$. Here, we also apply DOF$>$ 4, $\chi^2/\mathrm{Ndf} < 3$ quality cuts cuts on $\sim 4 \cdot 10^4$ events. The resolution can also be observed to range from ~ 30 % at $2 \cdot 10^{19}$ eV to 15–20 % at $\sim 10^{20}$ eV. Systematics have not been corrected and may still be contributing to the distribution width. In general, the energy resolution is not as good as in the case of events impinging in the center (Fig. 18). This is expected due to the wider set of conditions considered here with a wide range of systematics involved. Moreover, the events at the edges of the field of view are characterized by worse reconstruction performances due to the worsening detector quality. In Fig. 21, the fraction of events reconstructed with

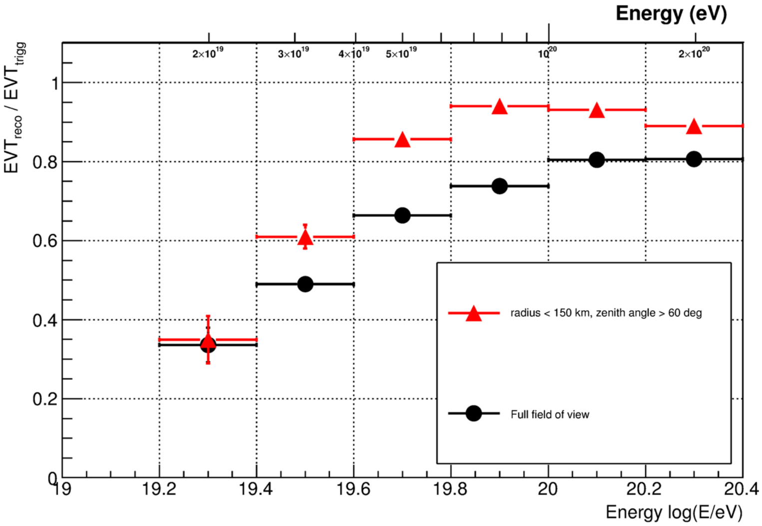

Fig. 21 The fraction of reconstructed events. We show here the fraction of events surviving the cut DOF > 4, $\chi^2/\mathrm{Ndf} < 3$. The fraction is shown with respect to the triggered events. In *black*, we see the full–FOV curve while, in *red*, the curve with the cut on the radial distance in the field of view (radius $<$ 150 km) and zenith angle $>$ 60 degrees

quality cuts DOF > 4 $\chi^2/\mathrm{Ndf} < 3$ with respect to triggered events is shown. As can be seen, the presence of such cuts delivers a fraction of reconstructed events which is reaching 80 % above $\sim 10^{20}$ eV. This fraction decreases to 35–40 % at $2 \cdot 10^{19}$ eV The application of cuts on the impact point position (radius from the center $<$ 150 km) and zenith angle (60 degrees) delivers a better reconstruction efficiency at the lowest energies. This is essentially due to the better optics properties (see Fig. 6 of [12]) in the center of the field of view and to the smaller shower–to–detector distance. As can be seen always in [12], the application of cuts on the field of view position and zenith angle will bring the trigger full efficiency range toward lower energies (90 % at 5–6 $\cdot 10^{19}$ eV). This reduces the systematics of the JEM–EUSO exposure at 4–5 $\cdot$ 10^{19} eV significantly. This allows a more reliable superposition with ground arrays. The reconstruction is also behaving in a similar way as the trigger studied in [12]. The exposure will, in fact, vary just up to 10 % if we consider energies of $5 \cdot 10^{19}$ eV. Further studies are needed but this result seems to show that the reconstruction is not hampering the superposition with ground arrays in a significant way.

In Fig. 22 we can see the impact points of all the successfully reconstructed events. The low (E $< 4 \cdot 10^{19}$ eV) and high energy (E $> 10^{20}$ eV) samples are represented in red and black respectively. As can be seen, low energy events are preferentially reconstructed when they impact in the central part of the field of view. On the other hand, high energy events, are of sufficient quality to be reconstructed everywhere. Some low energy event can, nevertheless, be reconstructed at the edges of the field

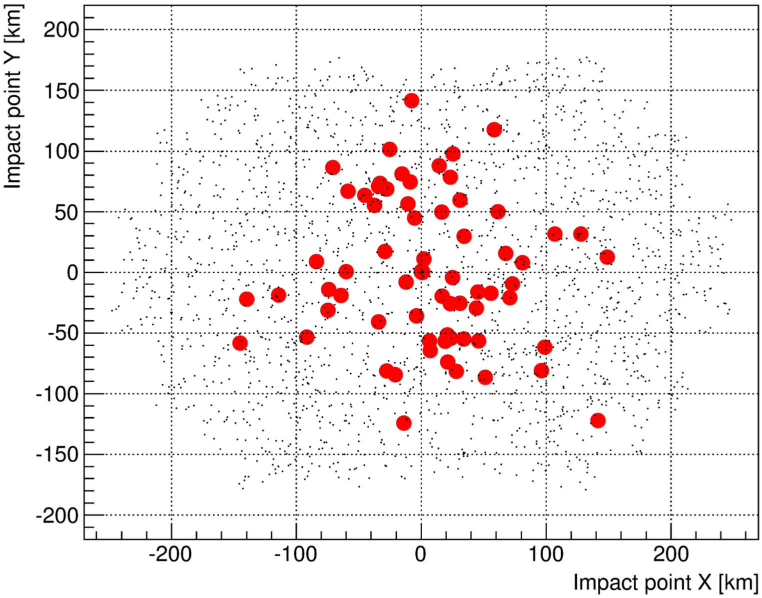

Fig. 22 the distribution of the impact points for the successfully reconstructed events is shown here. The slant depth method has been used. The events are distributed from 0 to 90 degrees in zenith angle. *Red dots* refer to events with E $< 4 \cdot 10^{19}$ eV *while black points* to E $> 10^{20}$ eV

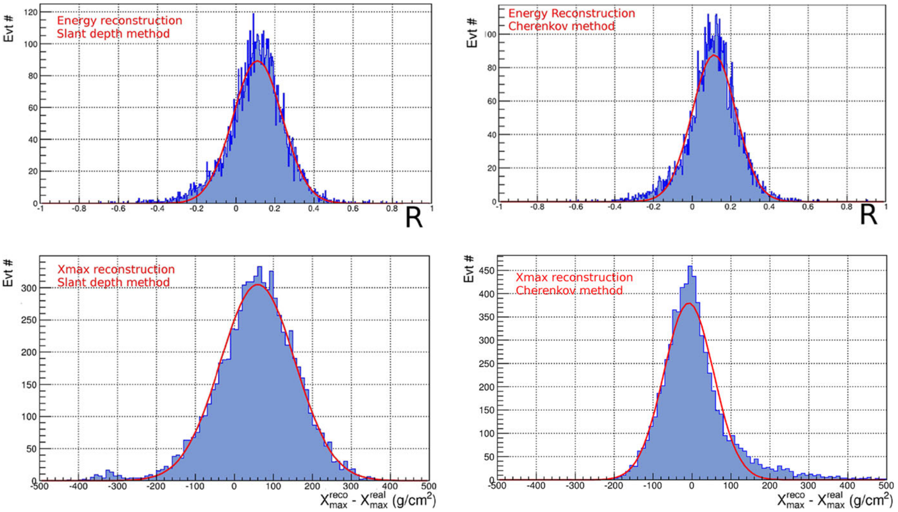

Fig. 23 We show here an example of the resolution distributions used for the plots of Figs. 18, 19, 24, and 25. We represent here just the distributions under one single condition (E = 10^{20} eV and zenith angle 45 degrees). The resolution distributions are shown here together with their Gaussian fit. All the plots are referring to the central part of the field of view (namely in the inner (±20, ±20) km)

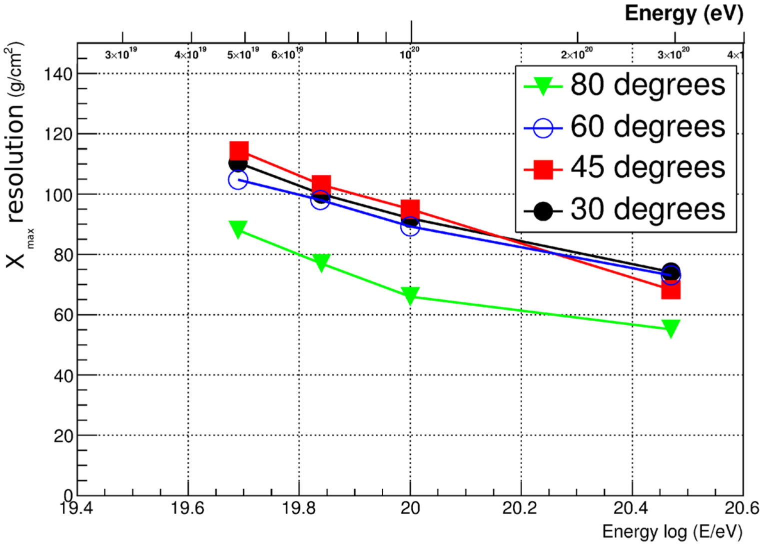

Fig. 24 The $X_{\max}$ resolution is shown here. Here we plot the results for various zenith angles and energies. All the events are impacting in the central part of the field of view (namely in the inner (±20, ±20) km). The geometry has been reconstructed with the slant depth method

of view. Such a subsample is represented by high zenith angle events. The higher altitude of their maxima makes, in fact, such events to be brighter and easier to be reconstructed.

4 $X_{\mathbf{max}}$ resolution

A similar study has been performed for the X_{max} parameter. Using the samples described in the previous section (like in Figs. 18 and 19), we have calculated the distribution of the slant depth of the maximum. In Figs. 24 and 25, we show the JEM–EUSO X_{max} resolution for fixed conditions of zenith angle and energy. Similarly as in the case for the energy, we evaluate the parameter $X_{\text{max}}^{\text{reco}} - X_{\text{max}}^{\text{real}}$ for all the events. We also fit the distribution with a Gaussian and we plot the σ parameter. This σ parameter defines the X_{max} resolution. An example of such distributions, with the corresponding Gaussian fit, can be seen in Fig. 23. More in detail in Fig. 24, we show the reconstruction performances for the slant depth method. As already explained in the previous sections, the result must be considered more as a test than the real performance estimation. In fact, the assumption on the $X_{\text{max}}^{\text{geo}}$ will cause a bias in the geometry reconstruction. The $X_{\text{max}}^{\text{fit}}$ plotted here will therefore be biased by the initial assumptions. The algorithm should be iterated in order to remove the dependence from any assumption. Nevertheless, this result can be seen as a proof of the establishment of the entire chain and as a test of the algorithms.

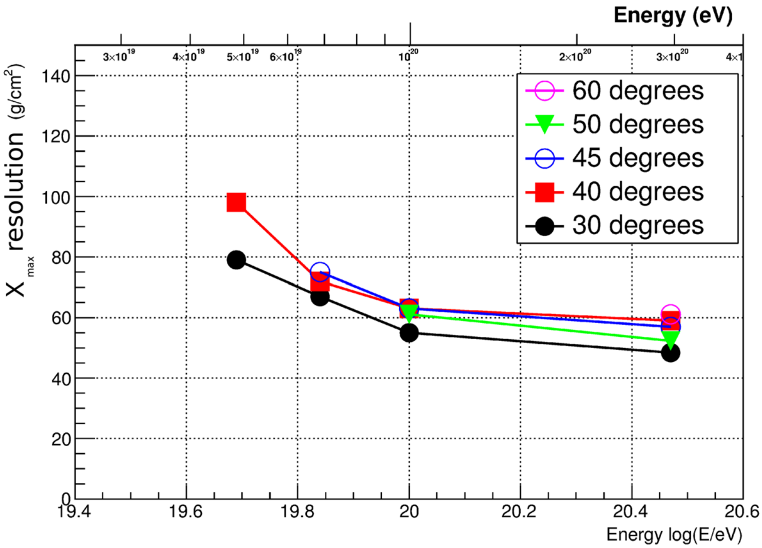

Fig. 25 The X_{max} resolution is shown here. Here we plot the results for various zenith angles and energies. All the events are impacting in the central part of the field of view (namely in the inner (±20, ±20) km). The geometry has been reconstructed with the Cherenkov method

As can be seen in Fig. 24, the $X_{\max}$ resolution improves with the energy. At the lowest energies, it ranges from 90 to 120 g/cm^2 while at the most extreme energies, from 60 to 80 g/cm^2. The higher zenith angles also bring a better resolution. This is due to the better angular resolution which can be achieved in these conditions. Moreover, the higher altitude of such events implies higher luminosities at the detector. The completeness of the profile can be also fitted and is not cut by the ground impact.

In Fig. 25, we can see the $X_{\max}$ reconstruction performances obtained with the Cherenkov method. As can be seen here, the performances are significantly better ranging from 80–100 g/cm^2 at the lowest energies and 50–60 g/cm^2 at the highest. As already explained, at the highest zenith angles the Cherenkov reflection peak will be not recognizable. For this reason, the plots will not extend above 60 degrees.

The highest energies also display a significantly better performance. However, unlike in the slant depth case, an improvement with the zenith angle cannot be seen. In fact, the quality of the Cherenkov peaks detected at large zenith angles is expected to decrease. In the most extreme cases, at low energies, these peaks will be affected by biases that prevent the $X_{\max}$ reconstruction. For this reason, a further selection has been performed in Fig. 25 and several points have been omitted. The $X_{\max}$ parameters is, in fact, much more sensible to systematics in the peak position than the energy and, therefore, several points that have been accepted in the energy reconstruction cannot be accepted for $X_{\max}$. The 45 and 50 degrees samples have only been shown for the highest energy cases.

The Cherenkov method is, however (where applicable), much more reliable since no assumption on the $X_{\max}^{\mathrm{geo}}$ is done in order to reconstruct the geometry. Such results can already be considered as a preliminary estimation of the JEM–EUSO $X_{\max}$ reconstruction capabilities.

5 Conclusions

Within this publication, the up–to–date JEM–EUSO energy and $X_{\max}$ reconstruction algorithms have been described. To test the reconstruction algorithms, some preliminary example has been shown in fixed conditions, both for the energy and for $X_{\max}$.

In fixed conditions, the energy resolution remains within ± 20 % above $5 \cdot 10^{19}$ eV for both slant depth and Cherenkov method. The resolution always improves with the energy reaching 5–10 % at $3 \cdot 10^{20}$ eV for both methods.

In fixed conditions $X_{\max}$ is generally reconstructed within ±120 g/cm^2 for the slant depth method and within ±100 g/cm^2 for the Cherenkov method. Here both algorithms also improve with the increasing energy reaching $\sim$ 50 g/cm^2 in both cases at $3 \cdot 10^{20}$ eV. The Cherenkov method will generally deliver a significantly better $X_{\max}$ resolution, especially for low zenith angles. The slant depth method gives an $X_{\max}$ resolution which improves with the zenith angle, while the Cherenkov method shows a roughly zenith angle–independent performance.

The detection of a Cherenkov mark will allow a better energy and $X_{\max}$ reconstruction and will offer the possibility of a cross calibration of the two methods. A subclass of events will be reconstructed with the Cherenkov method which presents the best performances. In all of the cases where no Cherenkov peak will be detected, the slant depth method will be used.

The energy reconstruction performances have also been studied on the entire FOV and for zenith angles from 0 to 90 degrees but only with the slant depth method. On the all–event sample (Fig. 20), the resolution is ±15 % at $2 \cdot 10^{20}$ eV, while at the lowest energies it is ±30 %. We compare these results with the ones obtained in the center, which are always below 20 %. The application of field of view cuts will, therefore, certainly improve the resolution.

In Fig. 21, an example of the reconstructed fraction after the application of basic cuts is shown as function of the energy on the all–events sample. As can be seen, around $5 \cdot 10^{19}$ eV between 65 % and 80 % of the triggered events can be reconstructed depending on the position and zenith angle selection cuts. The application of cuts on the impact position and on the zenith angle will deliver a higher efficiency at the lowest energies. This shows how a superposition with ground arrays is possible, however, more detailed studies are needed.

As can be seen, the requirements on the energy resolution mentioned in the introductory part are clearly satisfied. Above $8 \cdot 10^{19}$ eV we can, in fact, achieve less than ±25 % energy resolution against the ±30 % requirement. This performance is obtained on the whole FOV and on at least ~ 75 % of the triggered events.

However, the study on the $X_{\max}$ parameter is still not sufficient to conclude on the compliance with the requirement as it is referred just to the inner part of the field of view (±20, ±20) km. In fact, this part of the study was meant to prove the establishment of the algorithms for $X_{\max}$. A further, more complete, study will follow together with a dedicated optimization of the algorithms for $X_{\max}$. However, the reader must be aware of the fact that the resolution in the central part of the FOV is always smaller than the ±120 g/cm^2 requirement. Moreover, the JEM–EUSO detector will not immediately need the $X_{\max}$ reconstruction on the entire event sample. In fact, even fractions of the JEM–EUSO field of view could deliver much larger exposure than the fluorescence ground based detectors which are currently doing longitudinal development studies.

Acknowledgments We wish to thank the RIKEN Integrated Cluster of Clusters facility for the computer resources used for the calculations. We wish to thank the IPA program of RIKEN (Japan) for its support. This work has been partially supported by the Italian Ministry of Foreign Affairs, General Direction for the Cultural Promotion and Cooperation. We also wish to thank the original ESAF developers for their work.

References

1. Takahashi, Y., et al.: The JEM–EUSO mission. New J. Phys. **11**, 065009 (2009)
2. J. Adams et al. for the JEM–EUSO collaboration: Ultra High Energy Cosmic Rays studies with the JEM–EUSO mission, Experimental Astronomy Journal, this Issue's number 2 contribution
3. G.A. Medina Tanco for the JEM–EUSO collaboration: The JEM–EUSO Science capabilities. In: Proceeding of the Int. Cosmic Ray Conference (Rio De Janeiro), ID 0956 (2013)
4. T. Ebisuzaki et al. for the JEM–EUSO collaboration: The JEM–EUSO mission. Adv. Space Res. **53**, 1499–1505 (2014)
5. A. Santangelo for the JEM–EUSO collaboration: Status of the JEM–EUSO mission. In: Proceeding of the Int. Cosmic Ray Conference (Rio De Janeiro), ID 0956 (2013)

6. F. Kajino for the JEM–EUSO collaboration: The JEM–EUSO instruments. In: Proceeding of the Int. Cosmic Ray Conference (Rio De Janeiro), ID 1216 (2013)
7. Casolino, M., Kajino, F.: An overview of the JEM–EUSO instrument, this Issue's number 8 contribution
8. Dagoret, S., Barrillon, P., Jung, A., Ebersoldt, A.: The Photodetector Module of the JEM–EUSO mission, this Issue's number 9 contribution
9. The JEM–EUSO collaboration: Report on the phase A study 2010. Collaboration Mission Report (2010)
10. Berat, C., et al.: ESAF: Full simulation of space–based extensive air showers detectors. Astrop. Phys. **33**(4), 221–247 (2010)
11. Bertaina, M., et al.: Performance and air-shower reconstruction techniques for the JEM–EUSO mission. Adv. Space Res. **53**(10), 1515–1535
12. The JEM–EUSO collaboration: An evaluation of the exposure in nadir observation of the JEM–EUSO mission. Astroparticle Phys. **44**, 76–90 (2013)
13. Guzman, A., et al.: The peak and window searching technique for the EUSO simulation and analysis framework: Impact on the angular reconstruction of EAS. J. Phys. Conf. Series **409**, 012104 (2013)
14. Mernik, T., Guzman, A., Biktemerova, S.: Performances of JEM–EUSO: angular reconstruction, this Issue's number 10 contribution
15. Gora, D., et al.: Universal lateral distribution of energy deposit in air showers and its application to shower reconstruction. Astrop. Phys. **24**, 484–494 (2006)
16. National Oceanic Atmospheric Administration et al.: U.S standard atmosphere, 1976, public document (1976)
17. Giller, M., et al.: Energy spectra of electrons in the extensive air showers of ultra-high energy. J. Phys. G: Nucl. Part. Phys. **V**(30), P97–105 (2004)
18. Air Force Geophysics Laboratory, Users guide to LOWTRAN 7, public document (1988)
19. Nagano, M.: New measurement on photon yields from air and the application to the energy estimation of primary cosmic rays. arXiv:astro–ph/0406474v2 (2004)
20. Unger, M., et al.: Reconstruction of longitudinal profiles of ultra-high energy cosmic ray showers from fluorescence and Cherenkov light measurements. Nucl. Instr. Met. Phys. Res. A, 588 (2008)
21. Naumov, D.: SLAST, shower light attenuated to the space telescope. EUSO mission internal document (2003)
22. Rossi, B.: Cosmic–ray theory. K. Greisen Rev. Mod. Phys. **13**, 240 (1941)
23. Ilina, N.P., et al.: Sov. J. Nucl. Phys. **55**, 1540 (1992)
24. Kalmykov, N.N., Ostapchenko, S.S. Sov. J. Nucl. Phys. **50**, 315 (1989)
25. Fenu, F.: A simulation study of the JEM–EUSO mission for the detection of ultra–high energy Cosmic Rays, Doctoral Thesis (2013)

The JEM-EUSO Collaboration

J.H. Adams Jr.[md], S. Ahmad[bb], J.-N. Albert[ba], D. Allard[bc], L. Anchordoqui[mf], V. Andreev[me], A. Anzalone[dh,dn], Y. Arai[ev], K. Asano[et], M. Ave Pernas[kc], P. Baragatti[do], P. Barrillon[ba], T. Batsch[hc], J. Bayer[cd], R. Bechini[dl], T. Belenguer[kb], R. Bellotti[da,db], K. Belov[me], A.A. Berlind[mh], M. Bertaina[dk,dl], P.L. Biermann[cb], S. Biktemerova[ia], C. Blaksley[bc], N. Blanc[la], J. Błęcki[hd], S. Blin-Bondil[bb], J. Blümer[cb], P. Bobik[ja], M. Bogomilov[aa], M. Bonamente[md], M.S. Briggs[md], S. Briz[kd], A. Bruno[da], F. Cafagna[da], D. Campana[df], J-N. Capdevielle[bc], R. Caruso[dc,dn], M. Casolino[ew,di], C. Cassardo[dk,dl], G. Castellini[dd], C. Catalano[bd], O. Catalano[dh,dn], A. Cellino[dk,dm], M. Chikawa[ed], M.J. Christl[mg], D. Cline[me], V. Connaughton[md], L. Conti[do], G. Cordero[ga], H.J. Crawford[ma], R. Cremonini[dl], S. Csorna[mh], S. Dagoret-Campagne[ba], A.J. de Castro[kd], C. De Donato[di], C. de la Taille[bb], C. De Santis[di,dj], L. del Peral[kc], A. Dell'Oro[dk,dm] N. De Simone[di], M. Di Martino[dk,dm], G. Distratis[cd], F. Dulucq[bb], M. Dupieux[bd], A. Ebersoldt[cb], T. Ebisuzaki[ew], R. Engel[cb], S. Falk[cb], K. Fang[mb], F. Fenu[cd], I. Fernández-Gómez[kd], S. Ferrarese[dk,dl], D. Finco[do], M. Flamini[do], C. Fornaro[do], A. Franceschi[de], J. Fujimoto[ev], M. Fukushima[eg], P. Galeotti[dk,dl], G. Garipov[ic], J. Geary[md], G. Gelmini[me], G. Giraudo[dk], M. Gonchar[ia], C. González Alvarado[kb], P. Gorodetzky[bc], F. Guarino[df,dg], A. Guzmán[cd], Y. Hachisu[ew], B. Harlov[ib], A. Haungs[cb], J. Hernández Carretero[kc], K. Higashide[er,ew], D. Ikeda[eg], H. Ikeda[ep], N. Inoue[er], S. Inoue[eg], A. Insolia[dc,dn], F. Isgrò[df,dp], Y. Itow[en], E. Joven[ke], E.G. Judd[ma], A. Jung[fb], F. Kajino[ei],

T. Kajino[el], I. Kaneko[ew], Y. Karadzhov[aa], J. Karczmarczyk[hc], M. Karus[cb], K. Katahira[ew], K. Kawai[ew], Y. Kawasaki[ew], B. Keilhauer[cb], B.A. Khrenov[ic], Jeong-Sook Kim[fa], Soon-Wook Kim[fa], Sug-Whan Kim[fd], M. Kleifges[cb], P.A. Klimov[ic], D. Kolev[aa], I. Kreykenbohm[ca], K. Kudela[ja], Y. Kurihara[ev], A. Kusenko[me], E. Kuznetsov[md], M. Lacombe[bd], C. Lachaud[bc], J. Lee[fc], J. Licandro[ke], H. Lim[fc], F. López[kd], M.C. Maccarone[dh,dn], K. Mannheim[ce], D. Maravilla[ga], L. Marcelli[dj], A. Marini[de], O. Martinez[gc], G. Masciantonio[di,dj], K. Mase[ea], R. Matev[aa], G. Medina-Tanco[ga], T. Mernik[cd], H. Miyamoto[ba], Y. Miyazaki[ec], Y. Mizumoto[el], G. Modestino[de], A. Monaco[da,db], D. Monnier-Ragaigne[ba], J.A. Morales de los Ríos[ka,kc], C. Moretto[ba], V.S. Morozenko[ic], B. Mot[bd], T. Murakami[ef], M. Nagano[ec], M. Nagata[eh], S. Nagataki[ek], T. Nakamura[ej], T. Napolitano[de], D. Naumov[ia], R. Nava[ga], A. Neronov[lb], K. Nomoto[eu], T. Nonaka[eg], T. Ogawa[ew], S. Ogio[eo], H. Ohmori[ew], A.V. Olinto[mb], P. Orleański[hd], G. Osteria[df], M.I. Panasyuk[ic], E. Parizot[bc], I.H. Park[fc], H.W. Park[fc], B. Pastircak[ja], T. Patzak[bc], T. Paul[mf], C. Pennypacker[ma], S. Perez Cano[kc], T. Peter[lc], P. Picozza[di,dj,ew], T. Pierog[cb], L.W. Piotrowski[ew], S. Piraino[cd,dh], Z. Plebaniak[hc], A. Pollini[la], P. Prat[bc], G. Prévôt[bc], H. Prieto[kc], M. Putis[ja], P. Reardon[md], M. Reyes[ke], M. Ricci[de], I. Rodríguez[kd], M.D. Rodríguez Frías[kc], F. Ronga[de], M. Roth[cb], H. Rothkaehl[hd], G. Roudil[bd], I. Rusinov[aa], M. Rybczyński[ha], M.D. Sabau[kb], G. Sáez Cano[kc], H. Sagawa[eg], A. Saito[ej], N. Sakaki[cb], M. Sakata[ei], H. Salazar[gc], S. Sánchez[kd], A. Santangelo[cd], L. Santiago Crúz[ga], M. Sanz Palomino[kb], O. Saprykin[ib], F. Sarazin[mc], H. Sato[ei], M. Sato[es], T. Schanz[cd], H. Schieler[cb], V. Scotti[df,dg], A. Segreto[dh,dn], S. Selmane[bc], D. Semikoz[bc], M. Serra[ke], S. Sharakin[ic], T. Shibata[eq], H.M. Shimizu[em], K. Shinozaki[ew,cd], T. Shirahama[er], G. Siemieniec-Oziębło[hb], H.H. Silva López[ga], J. Sledd[mg], K. Słomińska[hd], A. Sobey[mg], T. Sugiyama[em], D. Supanitsky[ga], M. Suzuki[ep], B. Szabelska[hc], J. Szabelski[hc], F. Tajima[ee], N. Tajima[ew], T. Tajima[cc], Y. Takahashi[es], H. Takami[ev], M. Takeda[eg], Y. Takizawa[ew], C. Tenzer[cd], O. Tibolla[ce], L. Tkachev[ia], H. Tokuno[et], T. Tomida[ew], N. Tone[ew], S. Toscano[lb], F. Trillaud[ga], R. Tsenov[aa], Y. Tsunesada[et], K. Tsuno[ew], T. Tymieniecka[hc], Y. Uchihori[eb], M. Unger[cb], O. Vaduvescu[ke], J.F. Valdés-Galicia[ga], P. Vallania[dk,dm], L. Valore[df,dg], G. Vankova[aa], C. Vigorito[dk,dl], L. Villaseñor[gb], P. von Ballmoos[bd], S. Wada[ew], J. Watanabe[el], S. Watanabe[es], J. Watts Jr.[md], M. Weber[cb], T.J. Weiler[mh], T. Wibig[hc], L. Wiencke[mc], M. Wille[ca], J. Wilms[ca], Z. Włodarczyk[ha], T. Yamamoto[ei], Y. Yamamoto[ei], J. Yang[fb], H. Yano[ep], I.V. Yashin[ic], D. Yonetoku[ef], K. Yoshida[ei], S. Yoshida[ea], R. Young[mg], M.Yu. Zotov[ic], A. Zuccaro Marchi[ew]

[aa] St. Kliment Ohridski University of Sofia, Bulgaria
[ba] LAL, Univ Paris-Sud, CNRS/IN2P3, Orsay, France
[bb] Omega, Ecole Polytechnique, CNRS/IN2P3, Palaiseau, France
[bc] APC, Univ Paris Diderot, CNRS/IN2P3, CEA/Irfu, Obs. de Paris, Sorbonne Paris Cité, France
[bd] IRAP, Université de Toulouse, CNRS, Toulouse, France
[ca] ECAP, University of Erlangen-Nuremberg, Germany
[cb] Karlsruhe Institute of Technology (KIT), Germany
[cc] Ludwig Maximilian University, Munich, Germany
[cd] Inst. for Astronomy and Astrophysics, Kepler Center, University of Tübingen, Germany
[ce] Institut für Theoretische Physik und Astrophysik, University of Würzburg, Germany
[da] Istituto Nazionale di Fisica Nucleare - Sezione di Bari, Italy
[db] Universita' degli Studi di Bari Aldo Moro and INFN - Sezione di Bari, Italy
[dc] Dipartimento di Fisica e Astronomia - Universita' di Catania, Italy
[dd] Consiglio Nazionale delle Ricerche (CNR) - Ist. di Fisica Applicata Nello Carrara, Firenze, Italy
[de] Istituto Nazionale di Fisica Nucleare - Laboratori Nazionali di Frascati, Italy
[df] Istituto Nazionale di Fisica Nucleare - Sezione di Napoli, Italy
[dg] Universita' di Napoli Federico II - Dipartimento di Scienze Fisiche, Italy
[dh] INAF - Istituto di Astrofisica Spaziale e Fisica Cosmica di Palermo, Italy
[di] Istituto Nazionale di Fisica Nucleare - Sezione di Roma Tor Vergata, Italy
[dj] Universita' di Roma Tor Vergata - Dipartimento di Fisica, Roma, Italy
[dk] Istituto Nazionale di Fisica Nucleare - Sezione di Torino, Italy
[dl] Dipartimento di Fisica, Universita' di Torino, Italy
[dm] Osservatorio Astrofisico di Torino, Istituto Nazionale di Astrofisica, Italy
[dn] Istituto Nazionale di Fisica Nucleare - Sezione di Catania, Italy
[do] UTIU, Dipartimento di Ingegneria, Rome, Italy
[dp] DIETI, Universita' degli Studi di Napoli Federico II, Napoli, Italy

[ea] Chiba University, Chiba, Japan
[eb] National Institute of Radiological Sciences, Chiba, Japan
[ec] Fukui University of Technology, Fukui, Japan
[ed] Kinki University, Higashi-Osaka, Japan
[ee] Hiroshima University, Hiroshima, Japan
[ef] Kanazawa University, Kanazawa, Japan
[eg] Institute for Cosmic Ray Research, University of Tokyo, Kashiwa, Japan
[eh] Kobe University, Kobe, Japan
[ei] Konan University, Kobe, Japan
[ej] Kyoto University, Kyoto, Japan
[ek] Yukawa Institute, Kyoto University, Kyoto, Japan
[el] National Astronomical Observatory, Mitaka, Japan
[em] Nagoya University, Nagoya, Japan
[en] Solar-Terrestrial Environment Laboratory, Nagoya University, Nagoya, Japan
[eo] Graduate School of Science, Osaka City University, Japan
[ep] Institute of Space and Astronautical Science/JAXA, Sagamihara, Japan
[eq] Aoyama Gakuin University, Sagamihara, Japan
[er] Saitama University, Saitama, Japan
[es] Hokkaido University, Sapporo, Japan
[et] Interactive Research Center of Science, Tokyo Institute of Technology, Tokyo, Japan
[eu] University of Tokyo, Tokyo, Japan
[ev] High Energy Accelerator Research Organization (KEK), Tsukuba, Japan
[ew] RIKEN, Wako, Japan
[fa] Korea Astronomy and Space Science Institute (KASI), Daejeon, Republic of Korea
[fb] Ewha Womans University, Seoul, Republic of Korea
[fc] Sungkyunkwan University, Seoul, Republic of Korea
[fd] Center for Galaxy Evolution Research, Yonsei University, Seoul, Republic of Korea
[ga] Universidad Nacional Autónoma de México (UNAM), Mexico
[gb] Universidad Michoacana de San Nicolas de Hidalgo (UMSNH), Morelia, Mexico
[gc] Benemérita Universidad Autónoma de Puebla (BUAP), Mexico
[ha] Jan Kochanowski University, Institute of Physics, Kielce, Poland
[hb] Jagiellonian University, Astronomical Observatory, Krakow, Poland
[hc] National Centre for Nuclear Research, Lodz, Poland
[hd] Space Research Centre of the Polish Academy of Sciences (CBK), Warsaw, Poland
[ia] Joint Institute for Nuclear Research, Dubna, Russia
[ib] Central Research Institute of Machine Building, TsNIIMash, Korolev, Russia
[ic] Skobeltsyn Institute of Nuclear Physics, Lomonosov Moscow State University, Russia
[ja] Institute of Experimental Physics, Kosice, Slovakia
[ka] Consejo Superior de Investigaciones Científicas (CSIC), Madrid, Spain
[kb] Instituto Nacional de Técnica Aeroespacial (INTA), Madrid, Spain
[kc] Universidad de Alcalá (UAH), Madrid, Spain
[kd] Universidad Carlos III de Madrid, Spain
[ke] Instituto de Astrofísica de Canarias (IAC), Tenerife, Spain
[la] Swiss Center for Electronics and Microtechnology (CSEM), Neuchâtel, Switzerland
[lb] ISDC Data Centre for Astrophysics, Versoix, Switzerland
[lc] Institute for Atmospheric and Climate Science, ETH Zürich, Switzerland
[ma] Space Science Laboratory, University of California, Berkeley, USA
[mb] University of Chicago, USA
[mc] Colorado School of Mines, Golden, USA
[md] University of Alabama in Huntsville, Huntsville, USA
[me] University of California (UCLA), Los Angeles, USA
[mf] University of Wisconsin-Milwaukee, Milwaukee, USA
[mg] NASA - Marshall Space Flight Center, USA
[mh] Vanderbilt University, Nashville, USA